TU Delft

Delft University of Technology

Document Version
Final published version

Licence
CC BY

Citation (APA)
Damiani, N., Sharma, S., Bertassi, M., Smerilli, M., Mirra, M., Lanese, I., Parisi, E. R., O'Reilly, G. J., Messali, F., & Graziotti, F. (2026). Experimental out-of-plane seismic response of URM gables: Role of roof flexibility and differential input. *Engineering Structures*, *366*, Article 123376. https://doi.org/10.1016/j.engstruct.2026.123376

Important note
To cite this publication, please use the final published version (if applicable).
Please check the document version above.

Copyright
In case the licence states "Dutch Copyright Act (Article 25fa)", this publication was made available Green Open Access via the TU Delft Institutional Repository pursuant to Dutch Copyright Act (Article 25fa, the Taverne amendment). This provision does not affect copyright ownership.
Unless copyright is transferred by contract or statute, it remains with the copyright holder.

Sharing and reuse
Other than for strictly personal use, it is not permitted to download, forward or distribute the text or part of it, without the consent of the author(s) and/or copyright holder(s), unless the work is under an open content license such as Creative Commons.

Takedown policy
Please contact us and provide details if you believe this document breaches copyrights.
We will remove access to the work immediately and investigate your claim.

This work is downloaded from Delft University of Technology.

Engineering Structures 366 (2026) 123376

Contents lists available at ScienceDirect

Engineering Structures

journal homepage: www.elsevier.com/locate/engstruct

Experimental out-of-plane seismic response of URM gables: Role of roof flexibility and differential input

Nicolò Damiani [a,b,*], Satyadhrik Sharma [c,d], Marta Bertassi [e], Marco Smerilli [b,e], Michele Mirra [f], Igor Lanese [b], Elisa Rizzo Parisi [b], Gerard J. O'Reilly [e], Francesco Messali [d], Francesco Graziotti [a,b]

[a] Department of Civil Engineering and Architecture (DICAr), University of Pavia, Via Ferrata 3, Pavia 27100, Italy
[b] European Centre for Training and Research in Earthquake Engineering (EUCENTRE), Via Ferrata 1, Pavia 27100, Italy
[c] Netherlands Organisation for Applied Scientific Research (TNO), Delft 2629 JD, the Netherlands
[d] Department of Materials, Mechanics, Management & Design, Section of Applied Mechanics, Delft University of Technology (TU Delft), Stevinweg 1, Delft 2628 CN, the Netherlands
[e] University School for Advanced Studies IUSS Pavia, Piazza della Vittoria 15, Pavia 27100, Italy
[f] School of Architecture and Design, University of Camerino, Viale della Rimembranza 3, Ascoli Piceno 63100, Italy

ARTICLE INFO

Keywords:
Differential input motions
Gable walls
Incremental dynamic shake-table tests
Roof stiffness
Out of plane
Unreinforced masonry

ABSTRACT

Low-rise masonry buildings around the world often include unreinforced masonry (URM) walls combined with pitched roofs that are supported or enclosed by masonry gables. Such buildings constitute a significant portion of the built environment in several earthquake-prone regions, affected by either natural or induced seismicity. Masonry gables in these structures have repeatedly shown high seismic vulnerability to out-of-plane excitations, as documented in post-earthquake survey studies. This paper presents the main outcomes of an experimental campaign carried out within the ERIES-SUPREME project to increase the understanding in URM gable out-of-plane seismic response. Three full-scale, densely instrumented gable specimens were tested using a dual shake-table configuration and subjected to incremental dynamic excitations up to collapse, simulating both induced and tectonic earthquake scenarios. The experimental tests examined the influence of differential motions between the top and base of the gable wall, either linearly amplified or both amplified and out-of-phase, implemented by the two tables to reproduce the interaction with three distinct roof diaphragm configurations. Experimental results are discussed in terms of observed failure mechanisms, hysteretic force-displacement behaviour, as well as acceleration and displacement capacities. In particular, increasing roof diaphragm flexibility leads to earlier activation of the out-of-plane failure mechanism and to a marked reduction in collapse acceleration at the gable base, while the acceleration at ridge level provides a more consistent representation of the effective seismic demand acting on the gables.

1. Introduction

Low-rise masonry buildings in Europe and around the world are predominantly characterised by unreinforced masonry (URM) wall systems coupled with pitched roofs, often finished or supported by masonry gables. These structures comprise a significant portion of the building stock in seismic-prone regions, including areas affected by either natural seismic hazards or induced seismicity. Within these buildings, masonry gables are recurrently identified as the most seismically vulnerable components in the out-of-plane (OOP) direction. Post-earthquake damage surveys provide extensive evidence of this vulnerability. Field observations on ordinary URM buildings consistently report local OOP failures of gables and wall portions at building upper floors [1–16]. Similar damage patterns have been documented in historical masonry structures, particularly churches [17–21]. These observations indicate that gable vulnerability stems from multiple factors: pronounced slenderness, weak or insufficient connections to the roof structure, and their location at the building apex. This position exposes gables to seismic excitations whose frequency content and shaking properties are notably modified with respect to the input ground

* Corresponding author at: Department of Civil Engineering and Architecture (DICAr), University of Pavia, Via Ferrata 3, Pavia 27100, Italy.
E-mail address: nicolo.damiani@unipv.it (N. Damiani).

https://doi.org/10.1016/j.engstruct.2026.123376
Received 26 March 2026; Received in revised form 10 June 2026; Accepted 10 July 2026
Available online 23 July 2026
0141-0296/© 2026 The Author(s). Published by Elsevier Ltd. This is an open access article under the CC BY license (http://creativecommons.org/licenses/by/4.0/).

motion at the supporting structure foundation. Coupled with the fact that URM gables possess a very limited vertical overburden pressure, if any at all, this further increases their susceptibility to OOP instability. In addition, interaction with flexible roof diaphragms often aggravates gable vulnerability, as timber roof elements may filter and further amplify the transmitted seismic motion, as well as introduce an offset between the displacement demand applied to different heights of the gable. Despite the recognised importance of these issues, experimental data focusing specifically on the seismic performance of URM gables remain limited, with most available insights derived from tests on complete building systems rather than on isolated gables.

From a mechanical perspective, the OOP seismic capacity of URM walls, including gables, is predominantly governed by their geometric stability. Due to the low tensile strength of masonry, the potential presence of pre-existing damage, and the intrinsic slenderness of these elements, rocking-type failure mechanisms can be activated under relatively low seismic demand. The instability displacement predicted under static conditions could differ significantly from that developing under dynamic excitation [22,23], and a definitive relationship between the two has yet to be established. As a result, experimental shake-table tests are essential to properly characterise the OOP dynamic behaviour of URM gables under seismic loading. For gables in particular, the interaction with the connected roof-diaphragm structure may further and significantly influence their dynamic response for the reasons previously introduced.

While several dynamic experimental studies have been conducted on unreinforced masonry walls with rectangular geometries in one-way [24–27] and two-way [28–31] spanning configurations, research specifically addressing the OOP dynamic behaviour of masonry gables remains scarce in the published literature. A notable study about this topic was conducted by Tomasetti et al. [32], where a complete roof substructure, comprising URM gables resting on a reinforced-concrete floor slab and supporting a timber roof, was subjected to incremental dynamic shaking until the OOP collapse of the gables. Another relevant investigation was performed by Candeias et al. [33], who conducted dynamic shake-table tests on two scaled specimens constructed with brick and stone masonry. These specimens included a façade with a gable on top and two orthogonal return walls; however, roof and floor diaphragms were excluded from the experimental setup. Additionally, several experimental studies have focused on full-scale URM buildings with gables supporting roof structures [34–40]. However, these studies provided limited insights into the seismic OOP behaviour of gables for two key reasons: (i) alternative failure mechanisms often dominated the global seismic response of the building, preventing the OOP failure of gables (e.g., [40]); and (ii) even when roof or gable failure occurred as a precursor to other mechanisms, tests were frequently stopped before complete structural collapse, either for safety reasons or to avoid damage to the testing facilities (e.g., [36,37]), thereby limiting the quality of test observations up to and including full collapse.

To address these shortcomings, this paper presents results from a novel experimental test on the dynamic seismic behaviour of densely instrumented, full-scale URM gable walls tested to complete collapse. The tested specimens and their detailed material characterisation are described in Section 2. Although the roof diaphragm was not explicitly included in the experiments, its influence, particularly restraining effects, on the gable response was accounted for by applying differential input motions through an innovative experimental setup utilising two shake tables, one at the specimen base and the other at the gable top. This approach also results in idealised boundary conditions that can be readily reproduced in numerical models. Section 3 details the adopted test setup, the input motions (representative of both induced and tectonic earthquakes) applied to the two shake tables, and the incremental dynamic testing sequence. The achieved results are presented in Section 4, showcasing progression of damage, observed failure mechanisms, hysteretic force-displacement response, and acceleration-displacement capacity curves. Concluding remarks are finally drawn in Section 5.

The experimental dataset supporting these results, including comprehensive details of the testing setup, instrumentation schemes, material characterisation, as well as recorded displacement and acceleration time histories, is openly available for download from the Built Environment Data Experiments database [41] at https://doi.org/10.60756/euc−1avy7q49. The same dataset also includes videos of each test, providing a visual reference of the structural response throughout the testing sequence. Moreover, a companion data paper has been published to describe the dataset structure and contents and to provide guidance on its use [42]. These resources can serve as benchmarks for refining and calibrating numerical modelling approaches, as well as for developing new assessment tools. Overall, the generated dataset provides a foundation for future improvements to guidelines for the OOP seismic assessment of URM gables in existing buildings.

2. Description and material characterisation of the masonry specimens

2.1. Specimen geometry and details

The test specimens comprised nominally three identical, full-scale URM gable walls of triangular geometry, with a base length of 6.0 m and a height of 3.0 m, constructed on a composite steel-concrete foundation. Each masonry gable wall was built using solid clay bricks assembled in a single-wythe running-bond pattern with natural hydraulic lime (NHL 5) mortar. The bricks had nominal dimensions of 230 × 105 × 55 mm, resulting in a wall thickness of 105 mm. Each gable consisted of 45 brick courses with approximately 10-mm-thick mortar joints (Fig. 1). Five pockets were formed in the masonry to accommodate 300-mm-long timber purlins with a 100 × 200 mm cross-section. Each purlin was mechanically linked to the external test setup to replicate the boundary conditions of a continuous roof system, while transferring a vertical load of 4.5 kN (22.5 kN in total) to the gable, representing approximately half the weight of a typical timber roof diaphragm consistent with the tested geometry. This corresponded to an overburden of 71.4 kPa at gable mid-height cross section. The timber purlins also served as points for applying lateral input accelerations along the specimen height, as detailed in the following sections.

It is worth noting that steel anchors connecting roof-diaphragm purlins to masonry gables were intentionally omitted in this experimental campaign. Such anchorage systems are adopted in various construction practices to improve the connection between floor or roof diaphragms and masonry walls [43,44]. However, in a large portion of the existing masonry building stock their presence is often limited, inconsistent, or absent. Moreover, even when anchors are present, they may be inadequately designed or degraded over time, potentially leading to premature OOP failures [45]. Consequently, timber-to-masonry connections relied solely on friction, thus representing lower-bound boundary conditions for the seismic capacity of the gables by eliminating the potential restraining effect that such connectors could provide [46,47].

2.2. Material mechanical properties

Material characterisation tests were carried out to determine the mechanical properties of bricks, mortar, and masonry at the “Giorgio Macchi” Material and Structural Testing Laboratory of the Department of Civil Engineering and Architecture (DICAr) of the University of Pavia (Italy).

Brick compressive strength (f_b) and mortar compressive and flexural strengths (f_c , f_t) were obtained from compression and bending tests performed in accordance with EN 772–1 [48] and EN 1015–11 [49], respectively. Six masonry wallettes were loaded in compression perpendicular to the bed joints following EN 1052–1 [50], from which the masonry compressive strength (f_m) and secant elastic modulus (E_m), evaluated between 10% and 33% of f_m, were determined. The masonry

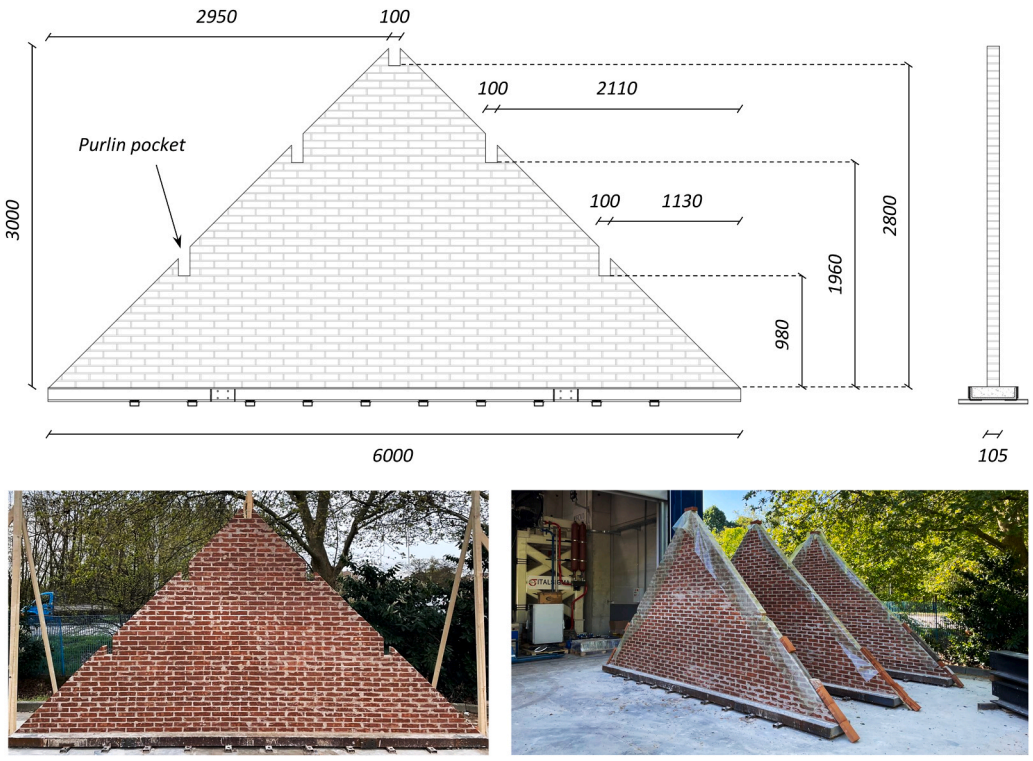


Fig. 1. Full-scale masonry gable specimen details and pictures. Units of mm.

shear parameters were quantified through direct shear tests on triplets in accordance with EN 1052–3 [51], yielding the initial shear strength (f_{v0}) and friction coefficient (μ). Bond wrench tests on masonry doublets, executed to EN 1052–5 [52], provided the bond strength (f_w). In addition, to characterise the response of bed joints under torsional shear stress ($f_{v0,tor}$, μ_{tor} evaluated assuming a linear elastic hypothesis) dedicated tests were conducted using the procedure proposed by Sharma et al. [53] to evaluate torsional shear capacity. The masonry density (ρ_m) was determined from the average weight of the three tested gables. Table 1 summarises the mean experimental values, coefficients of variation (CoV), and number of tested specimens for each investigated mechanical property. Additional information on the material characterisation campaign is freely available at https://doi.org/10.60756/euc-1avy7q49.

3. Experimental setup and dynamic loading sequence

The shake-table tests were conducted at the EUCENTRE laboratories (Pavia, Italy) using the 9D System. This seismic testing system employs a dual shake-table setup, featuring a top and bottom table, capable of imposing differential input motions across nine degrees of freedom. The bottom table is driven by actuators covering six degrees of freedom (three translations and three rotations), while the top table by actuators covering two translational and one rotational degree of freedom. This setup enables reproducing interstorey displacements that occur during earthquakes. The in-plane dimensions of the bottom shake table (i.e., 4.8 × 4.8 m) made it possible to test a full-scale gable but not a complete roof diaphragm structure. Accordingly, the influence of roof stiffness on the OOP seismic response of the gables was accounted for by varying the motion imposed at the top shaking table. Within the same experimental campaign, three distinct roof-gable interaction conditions were examined: (i) Gable1-STIFF, representing a stiff roof diaphragm, where the top shake table was controlled to replicate the motion of the bottom table; (ii) Gable2-SEMIFLEX, representing an intermediate case, with the top motion linearly amplified relative to the base; and (iii) Gable3-FLEX, simulating a flexible roof diaphragm, for which a different accelerogram was imposed at the top table, characterised by both higher amplitude and a different predominant period with respect to the base motion.

Table 1
Summary of masonry, unit and mortar mechanical properties.

Material properties	Symbol	Units	No. of tests [-]	Avg	CoV [-]
Mortar compressive strength	f_c	[MPa]	54	0.68	0.26
Mortar flexural strength	f_t	[MPa]	27	0.20	0.50
Unit/brick compressive strength	f_b	[MPa]	6	42.57	0.09
Masonry compressive strength	f_m	[MPa]	6	7.44	0.10
Masonry elastic modulus	E_m	[MPa]	6	4072	0.11
Masonry initial shear strength	f_{v0}	[MPa]	9	0.19	-
Masonry friction coefficient	μ	[-]	9	0.51	-
Masonry bond strength	f_w	[MPa]	19	0.21	0.48
Masonry initial shear strength (torsional)	$f_{v0,tor}$	[MPa]	9	0.42	-
Masonry friction coefficient (torsional)	μ_{tor}	[-]	9	1.15	-
Masonry density	ρ_m	[kg/m^3]	3	1883	-

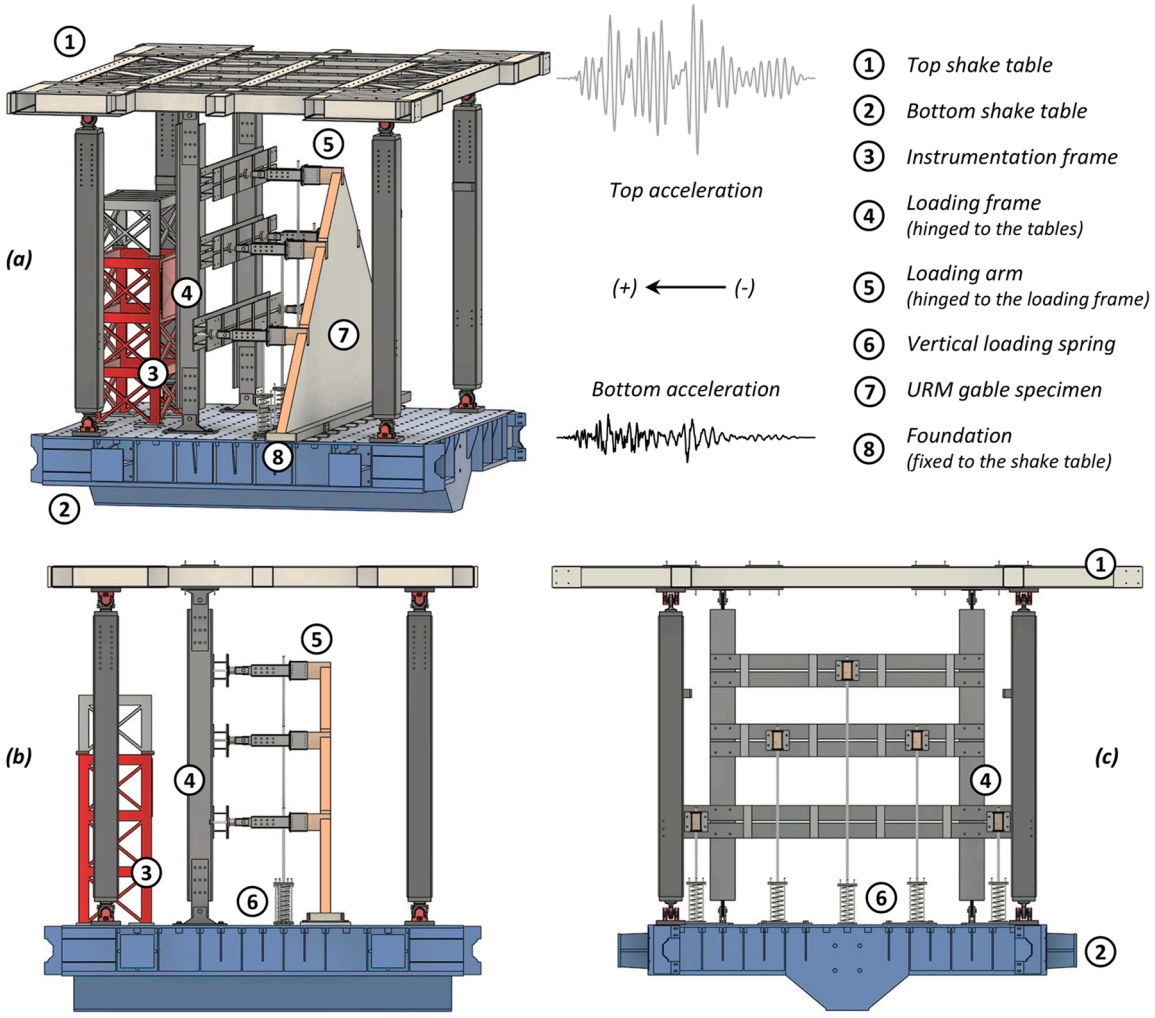


Fig. 2. (a) Three-dimensional, (b) lateral, and (c) front views of the adopted dual shake-table testing setup, including the direction of applied input motions.

3.1. Experimental setup

The experimental setup consisted of a dual shake-table configuration, with a top and bottom table capable of applying differential input motions (Fig. 2). An overview of the system, including the actuators driving the top table, is shown in Fig. 3a, b. A loading frame, assembled from tailored steel profiles, was employed to transmit the table accelerations along the gable height through five horizontal loading arms hinged to the frame (Fig. 3c, d). Timber members were screwed to the steel arms to replicate the timber purlins commonly found in roof structures (Fig. 3c, e). The loading frame was hinged to both the bottom and the top shake tables to accommodate the imposed relative displacements, without contributing additional OOP stiffness or strength to the specimens. The gable foundations were rigidly fixed to the bottom shake table. The testing setup was completed by a stiff instrumentation frame, rigidly anchored to the bottom table, which provided a stable support and reference for all instrumentation devices (Fig. 3a, b, d).

Vertical loads were applied to the gable specimens by pulling down the horizontal loading arms using steel bars in series with five springs, one for each loading arm (Fig. 3c). The spring pre-compression, set according to their stiffness, generated a downward force that was transferred through the steel arms, resulting in a vertical load of 4.5 kN applied to each timber purlin. The spring stiffness ($\approx$ 50 N/mm) was chosen to prevent excessive variations in the vertical load applied to the timber purlins, even as the gable approached collapse. The deformations and the corresponding vertical loads exerted by the springs on the timber purlins were continuously monitored throughout testing.

3.2. Instrumentation and data acquisition

Several accelerometers, displacement transducers, and a 3D optical acquisition system were installed on the gable specimens to monitor their responses [42]. The location of each instrument was selected based on the expected deformed shapes and cracking patterns of the gables. A total of 19 accelerometers, with measurement ranges of $\pm$ 2 g or $\pm$ 6 g, were used to record the acceleration time histories of the shake tables, masonry gables, timber purlins, and both the loading and instrumentation frames. Eleven linear potentiometers were employed to measure the elongation or shortening of vertical loading springs and the relative displacements between the timber purlins and the masonry. In addition, 13 wire potentiometers were installed on the gable specimens, loading frame, and instrumentation frame to capture the relative displacements of both the gables and the lateral loading system. Finally, the optical monitoring system, comprising 26 passive reflective markers, was used to measure displacements on the free surface of the gable (opposite from the loading frame) by tracking the marker trajectories through 10 high-definition cameras. Detailed descriptions and illustrations of the instrumentation setup for each gable specimen are openly available at https://doi.org/10.60756/euc-1avy7q49.



Fig. 3. Testing setup photos and details: (a) frontal view of the 9D dual shake-table system; (b) lateral view of the same system; (c) loading arm connected to spring device; (d) gable specimen with loading frame and instrumentation frame; (e) timber purlin seated in masonry pocket.

3.3. Input signals and testing sequence

The 9D System testing setup enabled independent control of the bottom and top shake tables, thereby reproducing differential input motions consistent with the in-plane stiffness of the roof diaphragm. Two floor-motion (FM) scenarios were considered: FM1, representative of induced seismicity, and FM2, associated with tectonic seismicity. For the induced seismicity scenario, a finite-element model of a typical URM building from the Groningen region (The Netherlands) was analysed considering three roof conditions: (i) as-built with a flexible timber diaphragm, (ii) retrofitted with a stiff concrete diaphragm, and (iii) retrofitted with a timber-based solution yielding a semi-flexible diaphragm. For the tectonic seismicity scenario, acceleration records obtained at the attic floor during the 2016 Central Italy earthquake in a monitored URM building were used; here, the roof-gable interaction was idealised by an elastic single-degree-of-freedom oscillator. The Dutch and Italian buildings served exclusively to derive representative floor-motion input signals associated with different seismic scenarios and target damage states at building level. Specifically, the input motion at the gable ridge level was first derived for each roof configuration: for the stiff roof, it was assumed equal to the attic-floor motion; for the semi-flexible roof, the same attic-floor accelerogram was amplified by a factor of ~1.7 for both FM1 and FM2, consistent with the numerically derived amplification ratio and the negligible phase shift observed for this scenario; for the flexible roof, a different accelerogram was adopted, incorporating both amplitude amplification and a phase shift with respect to the attic-floor signal, derived from the numerical analyses for FM1 and from the single-degree-of-freedom oscillator for FM2. The signal applied to the top shake table was then obtained by applying a geometrical correction accounting for the height difference between the top table and the actual gable ridge level. Further details on the selection and processing of the input signals can be found in Mirra et al. [54].

The induced and tectonic input motions applied at the bottom (i.e., attic floor) and top (i.e., ridge purlin) of the gables are shown in Fig. 4 together with their elastic acceleration and displacement response spectra for a 5% viscous damping ratio. Moreover, Table 2 summarises the nominal intensity measures of the selected motions at 100% intensity (scaling factor, SF, expressed as a percentage), including peak bottom acceleration (*PBA*), peak ridge acceleration (*PRA*), cumulative absolute velocity (*CAV*), Arias Intensity (I_A), Housner Intensity (I_H integrated between periods of 0.1 s and 2.5 s), 5%−95% significant duration (D_{5-95}), the period at peak spectral acceleration (T_d), and the peak absolute relative displacement between the ridge and the bottom of the gable (Δ_d). It is noted that, for the stiff roof configuration, the ridge input motion nominally coincides with the input motion at the bottom of the gable.

The sequence of input motions each gable specimen was subjected to, along with the respective scaling factors (linear scaling with respect to *PBA*), measured *PBA*, *PRA*, and Δ_d, is summarised in Table 3. The same table also reports the measured average spectral acceleration ($S_{a,avg}$) computed as the geometric mean of the spectral accelerations at the undamaged period of the gable (0.02 s) and at the maximum damaged-period value (0.66 s) [55]. The spectral accelerations were computed from an acceleration record obtained as the arithmetic mean of the gable-bottom and gable-ridge acceleration time histories. Further details on the choice of the selected period range are provided in Section 4.2.

The incremental dynamic test (IDT) for each gable specimen was conducted using both input signals (Table 3): first the induced sequence

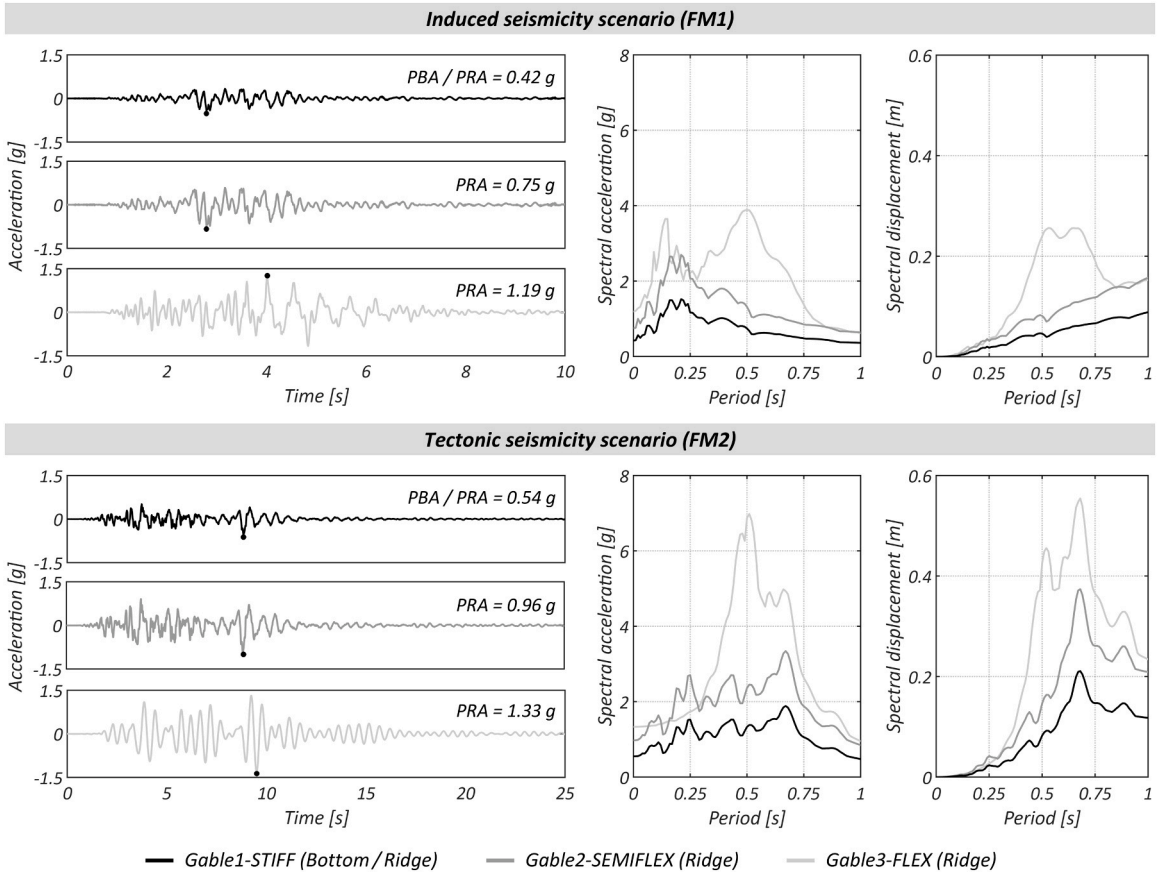


Fig. 4. Acceleration time histories (left) and elastic acceleration and displacement response spectra (centre, right) corresponding to FM1 (induced) and FM2 (tectonic) floor-motion scenarios.

Table 2
Nominal characteristics of the adopted input motions at SF = 100%.

Intensity measures	**Induced seismicity motions (FM1)**			**Tectonic seismicity motions (FM2)**		
	Gable bottom	Gable ridge		Gable bottom	Gable ridge	
	All roof scenarios	Semi-flexible	Flexible	All roof scenarios	Semi-flexible	Flexible
PBA [g]	0.42	-	-	0.54	-	-
PRA [g]	-	0.75	1.19	-	0.96	1.33
CAV [m/s]	5.35	9.48	17.6	14.3	25.3	47.2
I_A [m/s]	1.32	4.15	12.0	3.87	12.2	37.4
I_H [m]	0.95	1.69	2.24	1.41	2.50	3.44
D_{5-95} [s]	2.92	2.92	4.23	7.55	7.55	10.5
T_d [s]	0.22	0.22	0.50	0.66	0.66	0.50
Δ_d [mm]	-	25.4	56.8	-	42.5	82.2

(FM1), followed by the tectonic one (FM2). For FM1, the motions were scaled only up to 100%, as further amplification would have exceeded previously observed induced-seismic hazard levels, possibly introducing bias; the 100% FM1 motion was selected to be compatible with the uniform hazard spectrum corresponding to a 2475-year return period for a representative point in the Groningen region (The Netherlands), as described more in detail in [54]. To continue the IDT and push the specimens to collapse, the FM2 motions were then progressively scaled, starting from 50%, so as to ensure continuity between the two input scenarios while exploring higher shaking intensities and input records with different frequency content and longer durations. It is noted that for Gable3-FLEX an additional shake-table test at 100% FM1 (referred hereafter as Test #6-R) was conducted after Test #9 (i.e., the 100% FM2 run) to evaluate its ability to withstand an induced seismic motion after having sustained damage.

Before each IDT run, the specimens were carefully inspected, and the crack patterns were systematically mapped to monitor the progression of damage. A hammer-impact test was also performed at this stage, consisting of seven hammer blows distributed over the free façade of the gables (opposite to the loading frame), to excite the specimen and provide data for dynamic identification analyses. During these hammer tests, accelerometers were used to record the dynamic response. These tests were repeated before each IDT run to document the evolution of the gable dynamic properties throughout the testing sequence (Section 4.2).

Fig. 5 compares the target (theoretical) acceleration spectra with those computed from the measured acceleration time histories at the gable bottom and ridge for Tests #6 and #9, corresponding to 100% of FM1 and FM2 motions, respectively. All spectra were computed using a 5% damping ratio. As can be noted, the recorded acceleration spectra at the bottom of the gables (i.e., at the bottom shake table) show excellent

Table 3
Testing sequences adopted for incremental dynamic testing of the gable specimens. Values shown in bold correspond to the test at which collapse occurred for each specimen.

Test #	Input	SF	Gable1-STIFF				Gable2-SEMIFLEX				Gable3-FLEX			
			PBA [g]	*PRA* [g]	$S_{a,avg}$ [g]	Δ_d [mm]	*PBA* [g]	*PRA* [g]	$S_{a,avg}$ [g]	Δ_d [mm]	*PBA* [g]	*PRA* [g]	$S_{a,avg}$ [g]	Δ_d [mm]
1	FM1	10%	0.05	0.13	0.09	1.7	0.05	0.16	0.14	2.0	0.05	0.31	0.21	5.9
2	FM1	20%	0.08	0.19	0.20	1.6	0.08	0.29	0.28	4.4	0.09	0.53	0.37	12.1
3	FM1	30%	0.12	0.26	0.30	2.6	0.12	0.36	0.39	6.7	0.13	0.55	0.46	16.0
4	FM1	50%	0.19	0.39	0.48	4.6	0.20	0.45	0.63	10.6	0.20	0.84	0.73	26.7
5	FM1	75%	0.28	0.49	0.71	7.1	0.28	0.62	0.90	15.3	0.28	1.10	1.05	39.8
6	FM1	100%	0.37	0.61	0.92	8.9	0.38	0.81	1.17	19.9	0.36	1.33	1.37	52.8
7	FM2	50%	0.29	0.44	0.60	7.2	0.28	0.62	0.81	16.6	0.28	0.79	0.87	40.4
8	FM2	75%	0.43	0.53	0.87	10.5	0.42	0.93	1.18	24.1	0.43	1.28	1.35	57.0
9	FM2	100%	0.57	0.71	1.12	13.0	0.57	1.26	1.80	38.9	0.57	1.91	1.82	85.9
6-R	FM1	100%	-	-	-	-	-	-	-	-	0.36	1.33	1.37	53.9
10	FM2	125%	0.69	0.84	1.38	16.4	0.71	1.46	2.20	48.0	0.70	2.34	2.31	107.5
11	FM2	150%	0.86	0.96	1.64	19.3	0.86	1.86	2.62	56.9	**0.86**	**3.02**	**2.78**	**127.9**
12	FM2	175%	1.03	1.19	2.05	23.3	1.00	2.15	3.08	66.6				
13	FM2	200%	1.17	1.34	2.32	25.5	**1.17**	**3.31**	**3.53**	**75.4**				
14	FM2	250%	1.51	1.64	2.89	31.8								
15	FM2	300%	1.88	1.86	3.45	38.1								
16	FM2	350%	**2.33**	**2.56**	**3.97**	**43.1**								

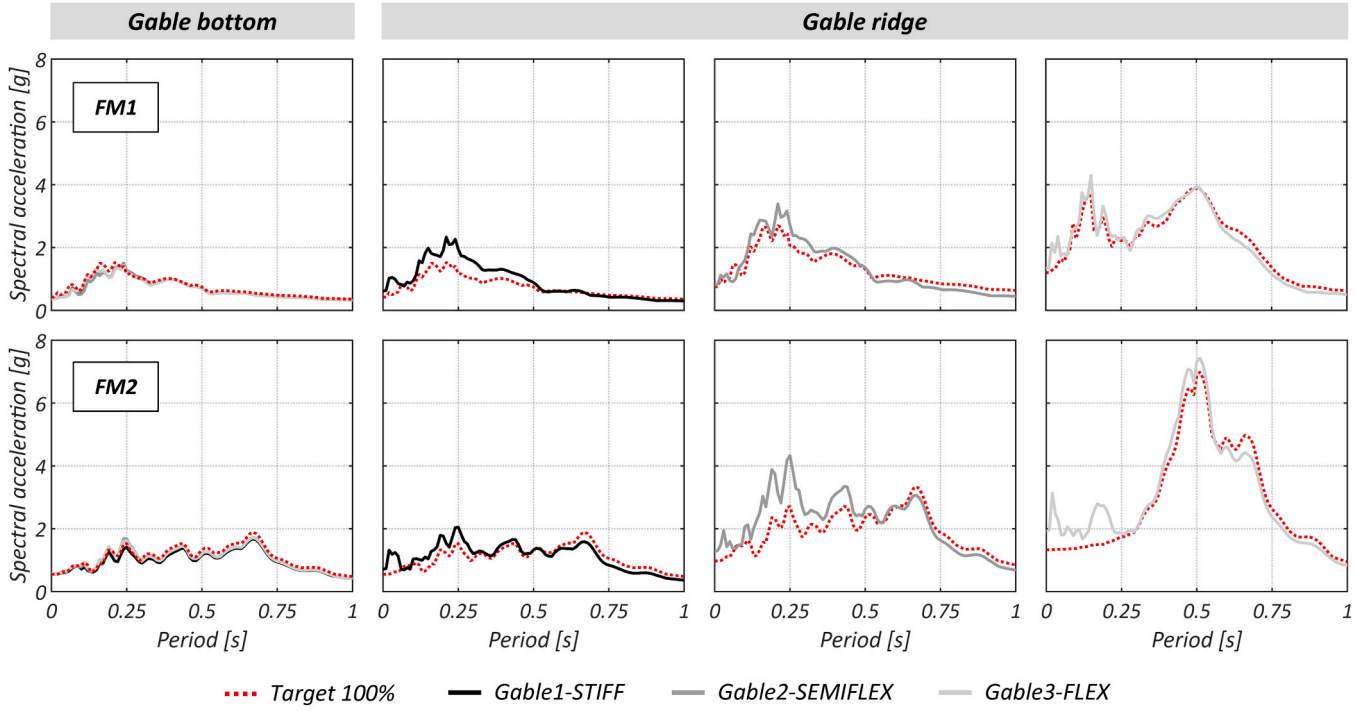


Fig. 5. Comparison between target (theoretical) and measured spectral accelerations at the gable bottom and ridge for Test #6 (100% FM1) and Test #9 (100% FM2).

agreement with the theoretical targets. At the gable ridge, however, minor discrepancies can be observed, reflecting the inherent difficulty of precisely controlling the motion of the top shake table, whose significantly lower mass makes it more sensitive to specimen-table dynamic interaction. Before installing the gable specimens, several pre-tests were carried out on the dual shake-table system to calibrate the

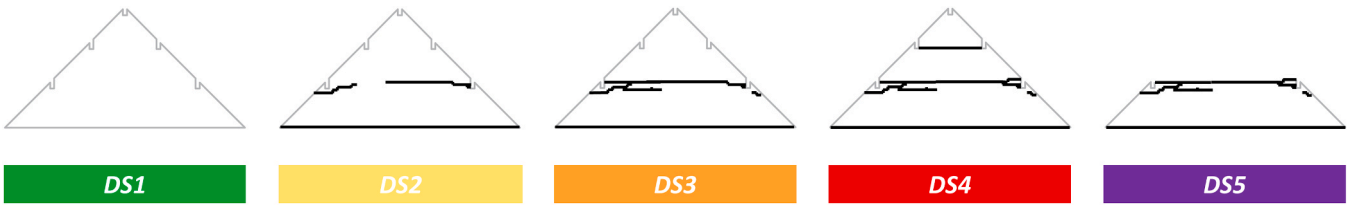


Fig. 6. Qualitative representation of DSs employed to describe damage progression in the specimens.

control parameters, ensuring that both the acceleration response spectra and the imposed Δ_d were consistent with the theoretical input motions. For Gable1-STIFF, the nominal value of Δ_d is zero (Table 2), since the ridge motion was intended to be identical to the motion at the gable bottom. However, this condition could not be reproduced exactly in the experiments due to the difficulty in achieving perfectly simultaneous movement of the bottom and top shake tables, particularly at low intensities. Consequently, non-zero values of Δ_d are observed throughout the Gable1-STIFF testing sequence (Table 3), indicating that the configuration is more realistically interpreted as a "stiff" rather than a perfectly "rigid" roof configuration.

4. Test results

The results of the three full-scale shake-table tests are presented in this section in terms of observed damage patterns and failure mechanisms, the evolution of gable dynamic properties throughout the testing sequence, hysteretic response, and acceleration capacities. Before discussing these aspects in detail, the condition of each gable at the end of each test was classified according to the following five damage states (DS) adapted from [28,31]: DS1, no visible structural damage; DS2, light structural damage; DS3, moderate structural damage without the full development of crack pattern corresponding to collapse mechanism; DS4, heavy structural damage with the full development of crack pattern corresponding to collapse mechanism; and DS5, very heavy structural damage with partial or global collapse of the gable.

Fig. 6 qualitatively illustrates the five DSs for a representative gable specimen; all three tested gables were ultimately pushed to DS5. It should be noted that, given the nature of dynamic testing, it was not always possible to identify a clear, sequential transition between consecutive DSs, particularly between DS3 and DS4; in many cases the specimens progressed through more than one DS within a single test.

In the following text, gable displacements are expressed in terms of the displacement of a control point (*CPD*), defined as the OOP displacement measured at the location on the gable that, for each test, experienced the largest deflection. The position of this control point was therefore allowed to vary from one test to the next, depending on the evolving deformation and damage patterns. Note that all *CPD*s reflect the actual gable deformation, excluding any rigid-body motion (Δ_d, Table 3) induced by the testing setup (i.e., the differential table input). Further details on the definition of this engineering demand parameter can be found in [42]. For consistency with the direction of the applied input motions (Fig. 2), positive displacement values indicate motion towards the loading frame, whereas negative values indicate motion away from it.

4.1. Damage patterns and failure mechanisms

The evolution of damage in the three gable specimens was characterised by a progressive intensification of cracking as the input motion intensity increased throughout the tests. Although the overall type and location of the main cracks remained broadly consistent during the tests, existing cracks widened and propagated, and additional secondary cracks formed as damage accumulated. After each test run, detailed damage mapping was performed to document the formation and propagation of cracks and to identify the onset of the collapse mechanism. All observed cracks are reported in this section together with the test in which they first appeared. In tests where the gable collapsed onto the shake table, the cracks responsible for the development of the failure mechanism were reconstructed from video recordings.

To aid the interpretation of the observed failure mechanisms, 3D deformed shapes of the gable surface were reconstructed. For each relevant test, a deformed shape was extracted, corresponding to the peak gable OOP displacement, as defined by the adopted sign convention (Fig. 2). These shapes were obtained by interpolating the measured displacements between the optical markers (indicated as black spheres) using a natural neighbour interpolation scheme over a triangular regular mesh defined on the gable surface. Each deformed shape is presented in two forms: (i) including the rigid-body motion induced by the differential table input, and (ii) with the rigid-body component removed to isolate the actual deformation of the gable wall. Videos documenting the full testing sequence, including the failure of each specimen, are available at https://doi.org/10.60756/euc-1avy7q49.

All three gable specimens exhibited a one-way bending OOP failure mechanism, with partial or complete collapse occurring through a three-body rocking mechanism with the formation of two main horizontal flexural cracks. These cracks extended across the full length of the gable and formed at the heights of the two rows of timber purlins, approximately 0.98 m and 1.96 m above the base (Fig. 7, Fig. 8, and Fig. 9). For all specimens, slight damage was first observed after Test #1 (10%

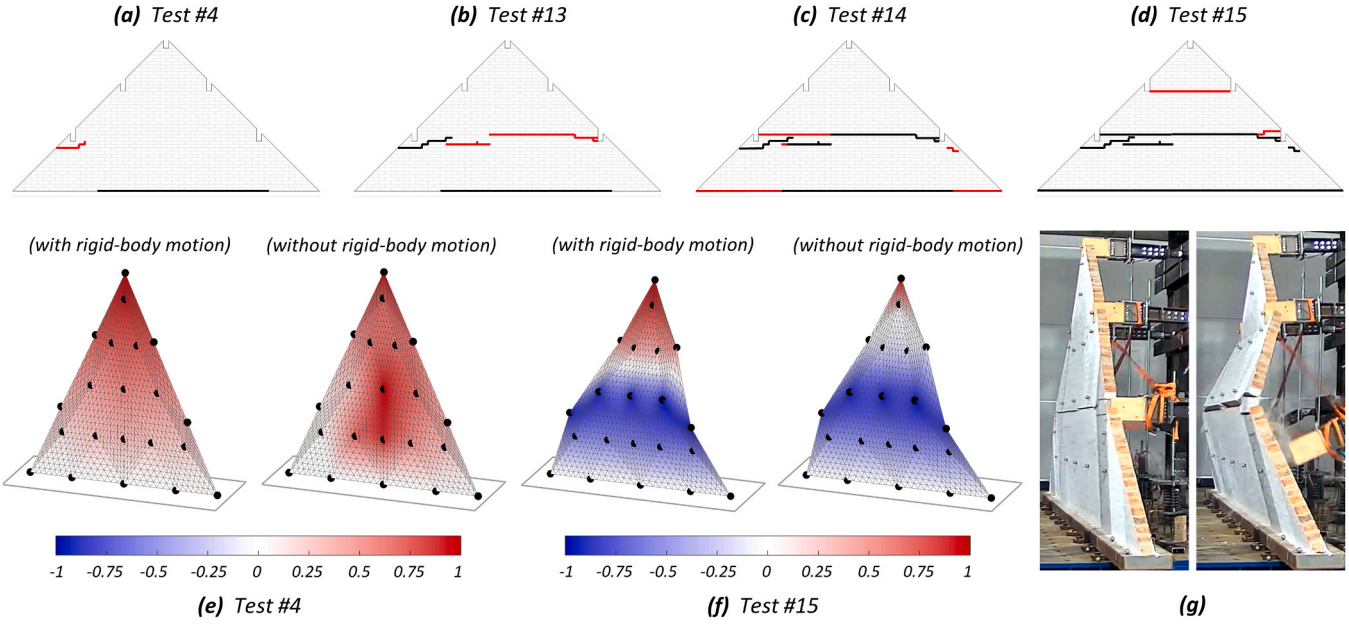


Fig. 7. Gable1-STIFF: evolution of the crack pattern (a–d); 3D deformed shapes with (left) and without (right) rigid-body motion at first cracking (Test #4) (e) and after the formation of failure mechanism (Test #15) (f); pictures of the collapse sequence (g).

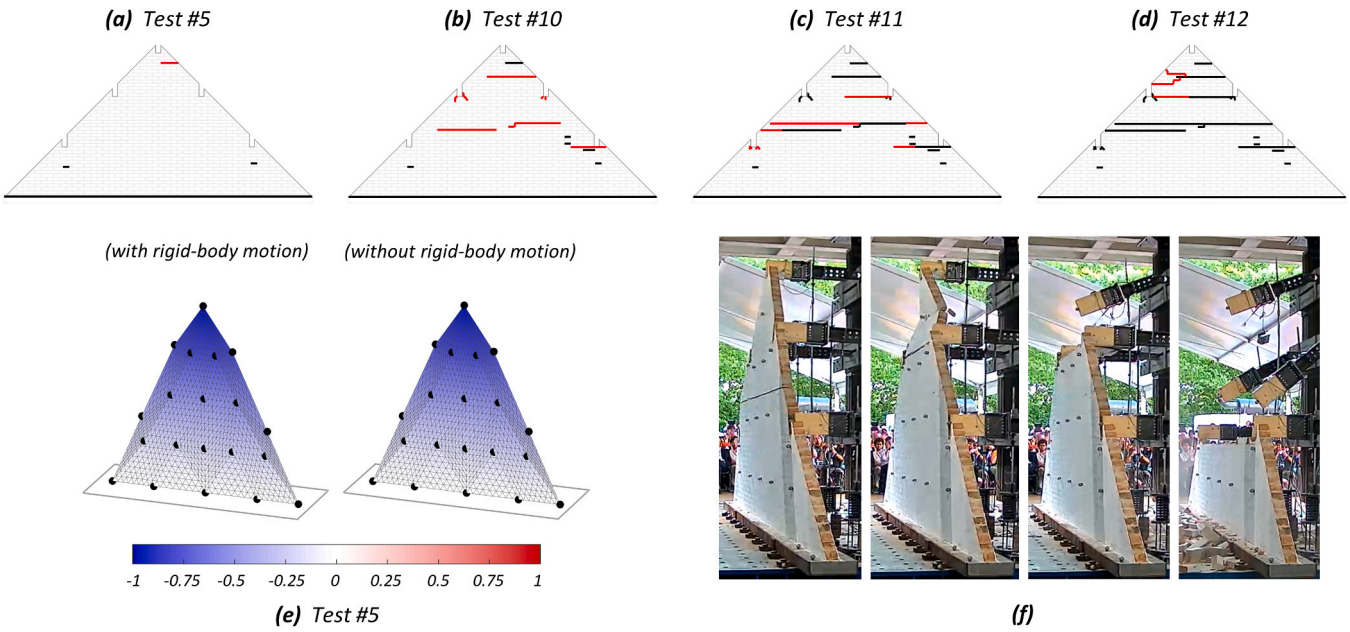


Fig. 8. Gable2-SEMIFLEX: evolution of the crack pattern (a–d); 3D deformed shapes with (left) and without (right) rigid-body rotation at first cracking (Test #5) (e); pictures of the collapse sequence (f). The 3D deformed shapes after the failure mechanism activation was not available due to disconnection of the optical acquisition system after Test #8.

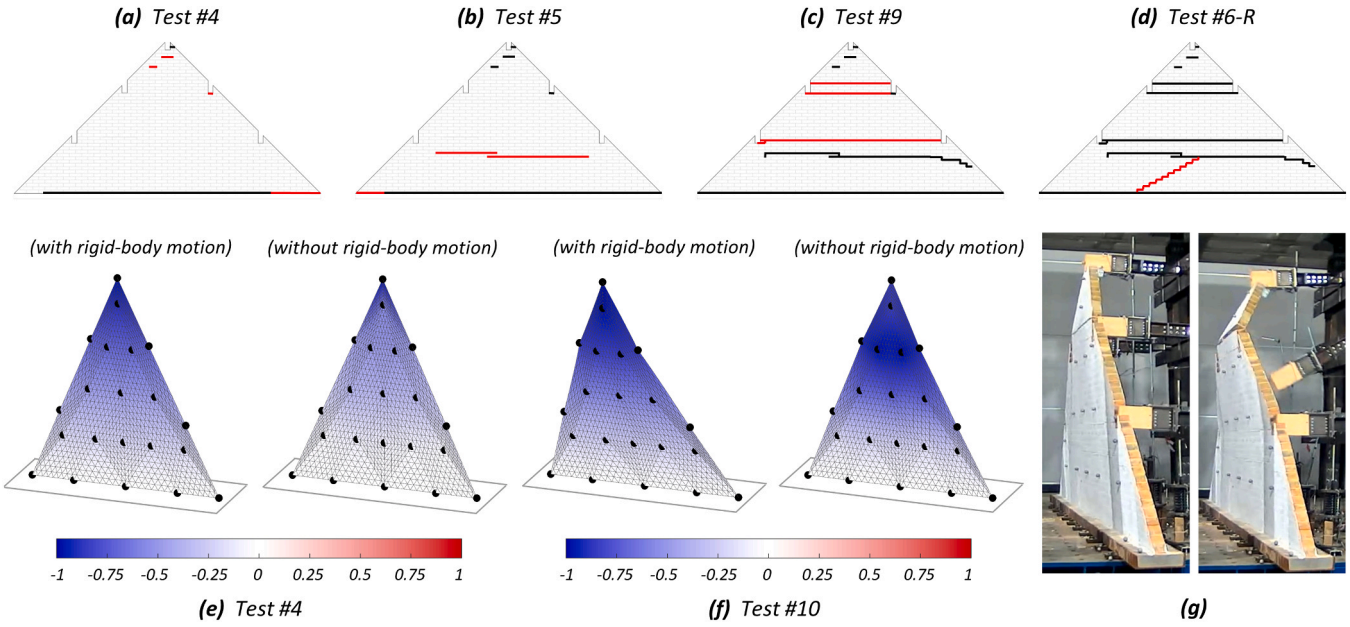


Fig. 9. Gable3-FLEX: evolution of the crack pattern (a–d); 3D deformed shapes with (left) and without (right) rigid-body motion at first cracking (Test #4) (e) and after the formation of failure mechanism (Test #10) (f); pictures of the collapse sequence (g).

FM1), consisting of the formation of a horizontal crack along the gable base. However, it remains uncertain whether this crack was induced by the initial seismic input or whether it was pre-existing, possibly formed during the lifting, handling, and positioning of the gable onto the shake table. The specimens were therefore still classified in DS1 after Test #1.

4.1.1. *Stiff roof configuration (Gable1-STIFF)*

Fig. 7 illustrates the damage evolution and failure mechanism of specimen Gable1-STIFF. In the reported crack patterns (corresponding to the gable façade opposite the loading frame), red lines indicate cracks that formed during the referenced test, whereas black lines denote cracks that had already formed in previous tests. Specimen Gable1-STIFF first exhibited slight damage, marking the transition from DS1 to DS2, after Test #4 ($PBA = 0.19$ g, $PRA = 0.39$ g, $\Delta_d = 4.6$ mm, peak $CPD = 0.3$ mm), when a horizontal crack developed beneath one of the lower-row timber purlins (Fig. 7a).

In subsequent tests, between Test #9 ($PBA = 0.57$ g, $PRA = 0.71$ g, $\Delta_d = 13.0$ mm, peak $CPD = 0.5$ mm) and Test #13 ($PBA = 1.17$ g, $PRA = 1.34$ g, $\Delta_d = 25.5$ mm, peak $CPD = -1.4$ mm), an additional horizontal crack developed below the purlin located at the opposite extremity of the same row. However, the specimen was still classified in DS2 because this second crack had not yet propagated across the full gable length and could therefore not act as an effective hinge line (Fig. 7b). The specimen transitioned to DS3 after Test #14 ($PBA = 1.51$ g, $PRA = 1.64$ g, $\Delta_d =$

31.8 mm, peak $CPD = 6.0$ mm). At this stage, the horizontal crack at the lower purlin level, together with the earlier crack at the gable base, had extended across the full width of the wall and began acting as hinge lines, enabling relative rocking between the upper and lower portions of the gable (Fig. 7c). Additional stepped and horizontal cracks developed around the pockets of the lower purlins, and noticeable sliding between the two purlins and the masonry was first observed during this test, indicating that the frictional resistance of the timber-masonry interfaces had been reached.

Test #15 ($PBA = 1.88$ g, $PRA = 1.86$ g, $\Delta_d = 38.1$ mm, peak $CPD = -48.5$ mm) caused further damage, including the complete formation of a second horizontal crack beneath the upper row of purlins (Fig. 7d). This new crack activated a secondary rocking mechanism, marking the transition from DS3 to DS4. Fig. 7e and f compare the deformed shapes of the gable specimen at first cracking and after the formation of the horizontal cracks responsible for initiating the OOP failure mechanism. Before the formation of the horizontal cracks connecting the purlin levels and triggering the one-way bending mechanism, the gable displayed a two-way bending deformed shape, with the peak CPD located approximately at its centroid (Fig. 7e). Once both hinge lines were fully formed, the response transitioned to one-way bending: the top gable portion, adjacent to the upper purlin row, remained nearly stationary, while most of the OOP displacements concentrated at the lower hinge line (Fig. 7f).

Ultimately, the gable reached DS5 and collapsed during Test #16 ($PBA = 2.33$ g, $PRA = 2.56$ g, $\Delta_d = 43.1$ mm). The collapse mechanism involved three-body rocking of the gable portions delineated by the horizontal cracks beneath the purlin rows, triggered by the pull-out of the lower purlin row from the masonry (Fig. 7g).

4.1.2. Semi-flexible roof configuration (Gable2-SEMIFLEX)

Fig. 8 illustrates the crack pattern evolution and failure mechanism of specimen Gable2-SEMIFLEX. This specimen exhibited visible damage, transitioning from DS1 to DS2, after Test #5 ($PBA = 0.28$ g, $PRA = 0.62$ g, $\Delta_d = 15.3$ mm, peak $CPD = 0.5$ mm), with only horizontal hairline cracks detected, in addition to the horizontal crack at the base already detected after Test #1 (Fig. 8a).

Fig. 8e shows the deformed shape at first cracking. Note that no optical data were available after Test #8, as the optical system was intentionally switched off; in fact, the second part of the IDT was performed live during the technical visit at the EUCENTRE laboratories organised as part of the World Conference on Earthquake Engineering (18th WCEE) held in Milan in July 2024, and the optical acquisition system is not compatible with the sunlight entering the laboratory when its external doors were fully opened to viewers.

Structural damage became more pronounced as the test progressed to higher input intensities. Significant crack formation occurred between the lower and upper sets of purlin pockets during Test #9 ($PBA = 0.57$ g, $PRA = 1.26$ g, $\Delta_d = 38.9$ mm, peak $CPD = -2.8$ mm) and Test #10 ($PBA = 0.71$ g, $PRA = 1.46$ g, $\Delta_d = 48.0$ mm, peak $CPD = -4.9$ mm). However, the specimen remained classified in DS2, as the horizontal cracking was still incomplete along the gable length and did not yet form fully effective hinge lines (Fig. 8b). During Test #10, non-negligible sliding (up to approximately 4 mm) was first observed between both the lower and upper pairs of purlins and the masonry, indicating full mobilisation of the frictional capacity at the timber-masonry interfaces.

After Test #11 ($PBA = 0.86$ g, $PRA = 1.86$ g, $\Delta_d = 56.9$ mm, peak $CPD = -8.7$ mm), new horizontal cracks developed and merged with the pre-existing one at mid-height, forming a continuous crack along the full gable length. Once continuous, this crack acted as a hinge line, marking the transition of the specimen into DS3 (Fig. 8c). In the upper part of the gable, additional horizontal cracks formed above and below the purlin pockets, although at this stage they were still discontinuous and had not yet propagated fully across the gable length. Residual sliding displacements of around 2 mm were observed between the upper pair of purlins and the masonry.

Test #12 ($PBA = 1.00$ g, $PRA = 2.15$ g, $\Delta_d = 66.6$ mm, peak $CPD = -29.9$ mm) produced further horizontal cracking in the upper portion of the gable, completing the propagation of previously initiated cracks along the full length. This test marked the complete formation of the failure mechanism and the transition to DS4 (Fig. 8d). After this test, residual sliding displacements up to about 15 mm were observed between the purlins and the masonry.

Finally, the specimen reached DS5 and partially collapsed during Test #13 ($PBA = 1.17$ g, $PRA = 3.31$ g, $\Delta_d = 75.4$ mm). The collapse mechanism, shown in Fig. 8f, involved rocking of the gable portions delineated by the horizontal cracks; in particular, the amplified rocking motion of the upper portion of the gable led to its overturning onto the shake table.

4.1.3. Flexible roof configuration (Gable3-FLEX)

Fig. 9 illustrates the damage evolution and failure mechanism observed for specimen Gable3-FLEX. For this specimen, the transition from DS1 to DS2 was observed after Test #4 ($PBA = 0.20$ g, $PRA = 0.84$ g, $\Delta_d = 26.7$ mm, peak $CPD = -1.2$ mm), when the horizontal crack along the gable base, partially detected after Test #1, extended further and additional hairline cracks formed in the upper portion of the gable (Fig. 9a). During Test #5 ($PBA = 0.28$ g, $PRA = 1.10$ g, $\Delta_d = 39.8$ mm, peak $CPD = -2.3$ mm) a new horizontal crack appeared in the central portion of the gable below the lower row of timber purlins, while the base crack propagated to span the full gable length (Fig. 9b).

Gable3-FLEX remained in DS2 up to Test #9 ($PBA = 0.57$ g, $PRA = 1.91$ g, $\Delta_d = 85.9$ mm, peak $CPD = -30.5$ mm). In this test, a marked increase in damage was observed. A continuous horizontal crack formed in the central part of the gable, connecting the bottoms of the lower purlin pockets and completing a hinge line at the lower purlin level. Simultaneously, two additional horizontal cracks developed in the upper portion of the gable, connecting the upper purlin row: one at the bottom and one at the top of the purlin pockets (Fig. 9c). The combined effect of these horizontal cracks led to the full development of the failure mechanism, analogous to that observed for Gable1-STIFF and Gable2-SEMIFLEX, resulting in the specimen transitioning directly from DS2 to DS4 within the same test. Moreover, significant residual sliding displacements of around 10 mm were observed between the lower and upper pairs of purlins and the masonry, indicating full mobilisation of the frictional resistance at the timber-masonry interfaces.

As discussed in Section 3.3, an additional shake-table test, denoted Test #6-R and corresponding to 100% FM1 ($PBA = 0.36$ g, $PRA = 1.33$ g, $\Delta_d = 53.9$ mm, peak $CPD = -22.3$ mm), was carried out after Test #9 to assess the ability of the damaged gable to sustain an induced-seismicity motion. This test did not cause significant additional damage and mainly led to the formation of an inclined stepped crack extending from the gable base to the horizontal crack developed during Test #5 (Fig. 9d).

Fig. 9e and f compare the deformed shapes of the specimen at first cracking and after the formation of the complete failure mechanism. Once the hinge lines were fully developed, the response transitioned to one-way bending, with the largest OOP displacements concentrated near the hinge line at the upper purlin level (Fig. 9f).

The specimen ultimately reached DS5 and partially collapsed during Test #11 ($PBA = 0.86$ g, $PRA = 3.02$ g, $\Delta_d = 127.9$ mm). The collapse mechanism was governed by the overturning of the two upper rigid bodies of the gable, located above the hinge line defined by the horizontal crack connecting the lower row of purlins, and was triggered by the pull-out of this lower row of purlins from the masonry leaf.

4.1.4. Damage state comparison

Fig. 10 compares the DS progression of the three gable specimens throughout the testing sequence, as a function of PBA and PRA. For any given test number, Gable1-STIFF, Gable2-SEMIFLEX, and Gable3-FLEX were subjected to the same bottom-table acceleration (Table 3),



Fig. 10. Relationship between experimental damage states and input intensity expressed in terms of (a) *PBA* and (b) *PRA* for the three gable specimens.

corresponding to an equivalent seismic demand at the attic-floor level in a real building context. Therefore, differences observed when DSs are plotted against *PBA* (Fig. 10a) directly reflect the influence of roof-diaphragm stiffness and of the resulting differential motion between gable base and ridge.

When expressed in terms of PBA, decreasing diaphragm stiffness leads to earlier activation of the OOP failure mechanism and faster progression toward collapse. Although all specimens first entered DS2 at relatively similar values of *PBA* levels, their subsequent evolution diverged markedly. Gable1-STIFF shows the slowest damage progression, with DS3, DS4 and DS5 attained at comparatively larger *PBA* values. Gable2-SEMIFLEX reached the same DSs at lower *PBA* levels, while Gable3-FLEX exhibited the earliest activation of the OOP mechanism and collapse at substantially reduced base accelerations.

When the same DSs are instead plotted against *PRA* (Fig. 10b), a different trend emerges. The *PRA* levels corresponding to DS3, DS4, and DS5 are much closer among the three specimens compared to the *PBA*-based representation. This reduced dispersion indicates that similar damage states are reached at comparable levels of acceleration at the gable ridge, despite the different base motions and roof-diaphragm conditions. This observation suggests that the acceleration at ridge level provides a more direct representation of the effective seismic demand governing OOP damage progression, at least for the tested configurations, where the roof-gable connection is governed by friction at the purlin-masonry interfaces. This aspect will be further discussed in Section 4.4.

4.2. Dynamic identification

Dynamic properties of the tested specimens, particularly the first natural mode of vibration, were continuously monitored throughout the IDTs. These properties provide a sensitive indicator of damage evolution, even when cracking is not yet detectable through visual inspection. The use of conventional white-noise input, commonly adopted for experimental modal identification [28,31], was not feasible due to the constraints of the dual-table configuration. Instead, the gable dynamic properties were assessed through hammer-impact tests performed before each IDT run, as described in Section 3.2.

Seven hammer blows were applied at predefined locations on the gable façade opposite the loading frame, including the timber purlins, as illustrated in Fig. 11a. The acceleration signals from each hammer test were processed by considering the accelerometer closest to the centre of gravity of the gables. Individual hammer blows were automatically detected and temporally isolated from the continuous acceleration time history to avoid overlap between consecutive impacts (Fig. 11b).

A Fourier transform was then applied to the cleanest isolated impact signal (i.e., the impulse exhibiting the highest signal-to-noise ratio and no interference from neighbouring blows) (Fig. 11c). The spectral analysis was restricted to a frequency band deemed appropriate for all specimens (i.e., 10–60 Hz), based on (i) the expected natural frequencies from pre-test numerical analyses and (ii) preliminary calibration tests on the dual-table setup with the loading and instrumentation frames installed but without the gable specimens.

Fig. 12 shows the evolution of the first-mode natural frequency for

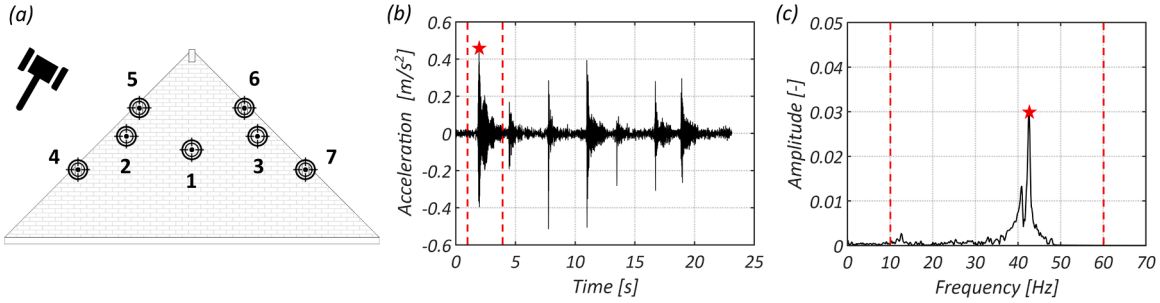


Fig. 11. Dynamic identification procedure (example for specimen Gable3-FLEX before Test #2): (a) sequence of the seven hammer blows; (b) recorded acceleration signal with isolation of the first hammer blow; (c) Fourier transform of the isolated signal showing the first vibration mode.

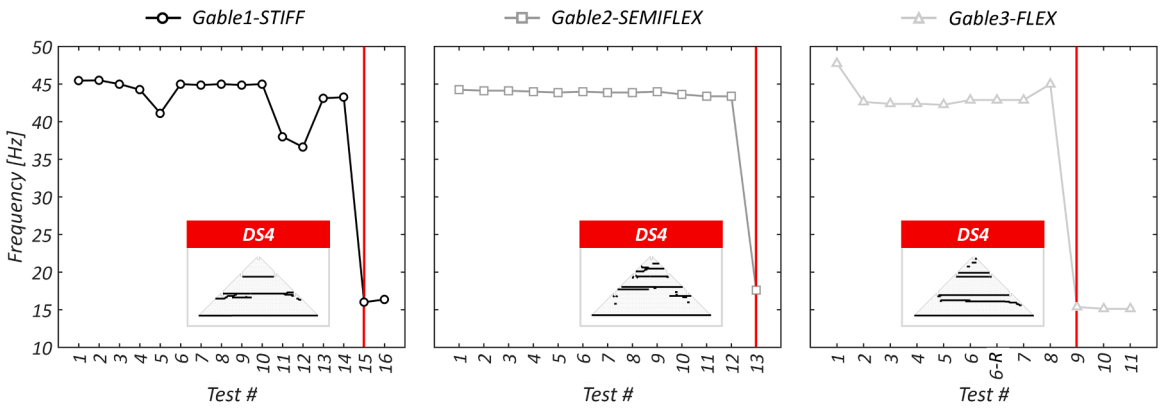


Fig. 12. First-mode natural frequencies identified before each IDT for Gable1-STIFF, Gable2-SEMIFLEX, and Gable3-FLEX. The red vertical line marks the test at which DS4 (full failure mechanism formation) was reached.

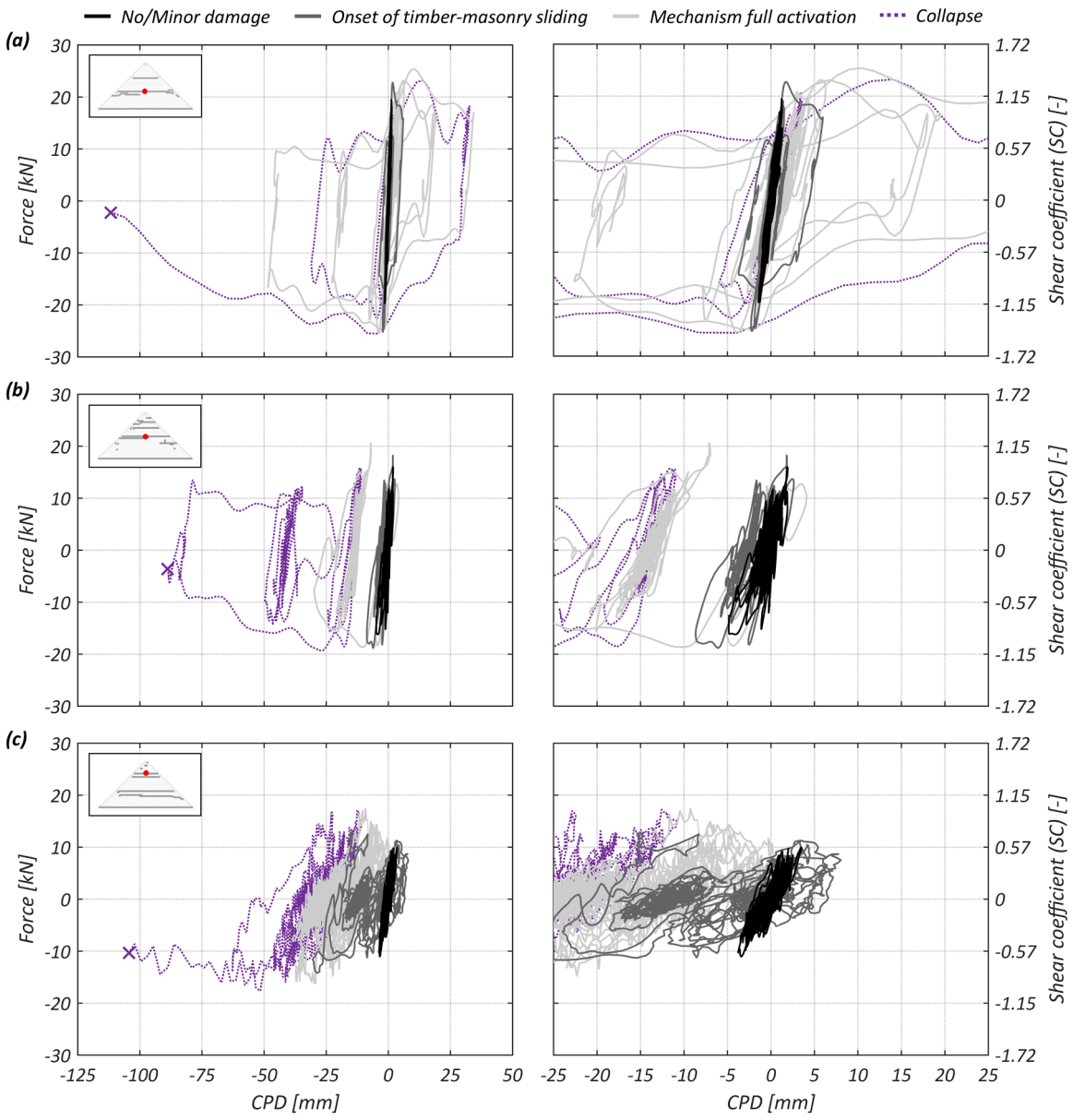


Fig. 13. Hysteretic response of gable specimens (location of *CPD* indicated by red dot [42]); the plots in the right column show close-up views of the same hysteretic loops shown in the left column: (a) Gable1-STIFF; (b) Gable2-SEMIFLEX; (c) Gable3-FLEX.

the three gables, obtained with the hammer-test procedure described above. Two distinct frequency ranges can be identified, corresponding to the stages before and after the full activation of the collapse mechanism (see previous section). Prior to the development of the complete mechanism, the fundamental frequency of the gables, apart from a few outliers, remained close to its initial value measured before Test #1, with values generally between 40 and 45 Hz (i.e., periods (T) between 0.022 s and 0.025 s). These results are consistent with linear-elastic eigenvalue analyses performed on the gable specimens using both shell finite-element (Midas Gen [56]) and discrete-element models (3DEC [57]).

Once the full rocking failure mechanism had formed (corresponding to the transition into DS4) a clear frequency drop was observed for all specimens, with the first-mode frequency reducing to approximately 15 Hz ($T \approx 0.07$ s) and remaining roughly constant up to collapse. It is important to emphasise that this frequency does not represent the rocking frequency of the multi-block mechanism and therefore does not correspond to the maximum damaged period of the gables. Throughout the dynamic tests, the response was continuously forced by the imposed input motions and affected by frictional interaction between the timber purlins and the masonry, so that a free-rocking frequency could not be reliably extracted. For this reason, when defining $S_{a,avg}$, an upper-bound damaged period of 0.66 s was adopted instead, taken as the period at which the spectral acceleration of the input motions reached its maximum over all performed tests.

4.3. Hysteretic behaviour

The hysteretic response of each gable specimen is illustrated in Fig. 13, in terms of inertial force and shear coefficient (SC) versus *CPD*, defined as the out-of-plane displacement measured at the control point after removing the rigid-body motion induced by the imposed differential displacement between the top and bottom shake tables (Δ_d, Table 3). Time-histories of inertial forces were obtained by multiplying the acceleration recorded by accelerometers by the corresponding tributary mass, assuming lumped masses at the accelerometer locations. The tributary masses assigned to each accelerometer were updated throughout the IDT to reflect the evolution of damage and crack patterns. Full details on the inertial-force computation and on the tributary areas associated with each accelerometer for all three gables are provided in [42]. The *SC* was calculated by dividing the inertial forces by g (acceleration due to gravity) and by the total mass of the gables, taken as the self-weight of the specimen (1.78 t). For each specimen, Fig. 13 also includes a close-up view of the small-displacement range, allowing a clearer appreciation of the shape of the small-displacement hysteretic loops.

The hysteretic response of each specimen was subdivided into four phases, superimposed in the plots using different colours and line styles. The first phase includes the runs in which no damage or only minor damage occurred (i.e., up to DS2), with the gable remaining almost elastic. The second phase corresponds to the run marking the onset of moderate damage (i.e., attainment of DS3), associated with the initiation of relevant sliding between the masonry and the timber purlins, and the transition to non-linear response ranges. The third phase comprises the testing runs in which the complete OOP failure mechanism was activated (i.e., DS4). Finally, the fourth phase corresponds to the final testing run associated with partial or complete collapse of the gable (DS5).

For Gable1-STIFF (Fig. 13a), the response was initially almost elastic, with narrow hysteretic loops and only minor damage up to Test #13, before the formation of the horizontal cracks associated with the OOP failure mechanism. A marked change in the hysteresis was observed during Test #14, when sliding between the masonry and the timber purlins initiated: the hysteretic cycles became significantly wider, indicating increased energy dissipation primarily governed by friction at the timber-masonry interfaces. The complete OOP failure mechanism developed in the subsequent run (Test #15), while collapse occurred during Test #16. Throughout these latter stages (Tests #14–16), most of the energy dissipation was provided by frictional sliding between the timber purlins and the masonry, as evidenced by the wide loops with stiff unloading and reloading branches.

Similarly, for Gable2-SEMIFLEX (Fig. 13b), the response was almost elastic up to Test #11, with slightly larger energy dissipation than for Gable1-STIFF. A marked change in the hysteresis was observed during Test #12, when sliding between the masonry and the timber purlins initiated. In this case, however, significant residual sliding displacements developed, producing residual offsets of the hysteretic loops that became even more evident in Test #13 (when the complete failure mechanism was activated) and Test #14 (partial collapse). In the final run, wide hysteretic loops, similar to those observed for Gable1-STIFF, could be seen.

Finally, Gable3-FLEX (Fig. 13c) exhibited an almost elastic response up to Test #8, with narrow hysteretic loops and limited damage. A marked transition to non-linear behaviour was observed during Test #9, when significant sliding displacements between the timber purlins and the masonry developed, producing noticeable residual offsets of the hysteretic loops in the negative displacement direction. The complete OOP failure mechanism was activated in the subsequent run (Test #10) and was accompanied by progressively increasing residual sliding displacements. Collapse occurred during Test #11.

All specimens exhibited a broadly similar hysteretic response. In all three cases, an initial phase of almost elastic response was observed, followed by a transition to non-linear behaviour governed by the mobilisation of friction at the timber-masonry interfaces. In the case of Gable1-STIFF, no significant residual *CPD* attributable to unrecovered timber-masonry sliding was observed, in contrast to the response of the other two gables, which developed appreciable residual offsets. The peak inertial forces reached in the tests were 25.5 kN ($SC = 1.46$) for Gable1-STIFF, 20.6 kN ($SC = 1.18$) for Gable2-SEMIFLEX and 17.7 kN ($SC = 1.01$) for Gable3-FLEX. These values are of the same order of magnitude and are largely controlled by the frictional resistance between the timber purlins and the masonry, estimated to lie between approximately 11 kN and 16 kN by assuming a friction coefficient in the range 0.5–0.7. The remaining portion of the total inertial force is then associated with the lateral forces transmitted to the base of the masonry gables.

Beyond the similarities in peak strength, Fig. 13 highlights clear differences in cyclic stiffness degradation among the three configurations. Gable1-STIFF and Gable2-SEMIFLEX display comparable initial stiffness and similar slopes of the hysteretic branches within the low-damage range, whereas Gable3-FLEX exhibits a markedly lower secant stiffness once cracking and sliding initiate, resulting in less steep and more distorted hysteretic loops. The increasing flexibility of the roof diaphragm therefore results in earlier stiffness loss and reduced cyclic stability. Moreover, the residual offsets visible in the loops of Gable2-SEMIFLEX and, more prominently, Gable3-FLEX indicate cumulative unrecovered sliding in a consistent displacement direction (away from the loading frame), evidencing a progressive loss of compatibility between the masonry and the roof purlins. The close-up views in Fig. 13 further reveal small but detectable deviations from linearity in the early cycles, particularly for Gable2-SEMIFLEX and Gable3-FLEX, which precede the formation of continuous hinge lines and confirm the role of interface friction in triggering non-linear behaviour.

Independently of roof stiffness, the *CPD*-based hysteretic plots (with rigid-body rotation removed) show that all specimens reached very similar displacement levels at the onset of instability, marked with an "X" in Fig. 13. The instability displacement was defined as the last measured *CPD* value immediately prior to partial or global collapse of the specimen. The instability *CPD* was approximately −112 mm for Gable1-STIFF, −89 mm for Gable2-SEMIFLEX, and −104 mm for Gable3-FLEX. Notably, Gable1-STIFF exhibited a clear negative-stiffness branch immediately prior to loss of equilibrium, a characteristic feature

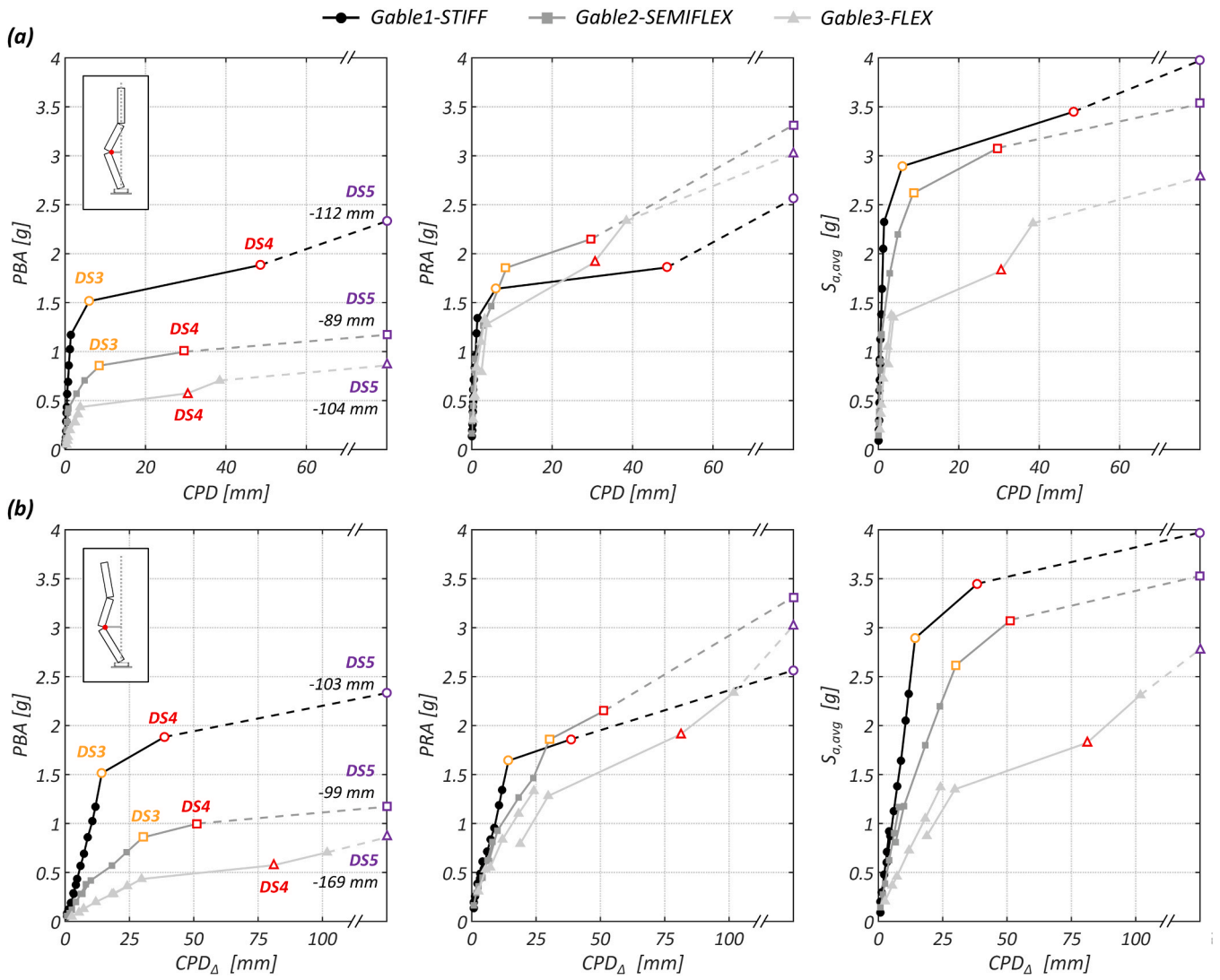


Fig. 14. Specimen capacities in terms of experimental *PBA*, *PRA*, and $S_{a,avg}$ versus peak control-point displacement: (a) *CPD* (gable deformation only); (b) CPD_Δ (gable deformation plus rigid-body motion).

of OOP rocking response. The fact that these critical displacement values are of the same order, and close to the wall thickness, is consistent with the expected behaviour of one-way rocking mechanisms in masonry walls. The slightly smaller value recorded for Gable2-SEMIFLEX is attributed to the observed collapse mechanism: during the final testing run, the upper portion of the gable overturned (Fig. 8) before the portion associated with the control point reached displacement levels comparable to those measured in the other two specimens. For Gable3-FLEX, residual inertial forces of approximately 10 kN were still recorded after partial collapse. Unlike Gable1-STIFF, which experienced a global collapse resulting in a near-zero inertial force, the flexible configuration retained a stable lower portion after overturning of the upper portions. The accelerometers installed on this remaining part continued to record acceleration, leading to non-zero residual inertial forces.

4.4. Capacity curves and intensity measure dependence

Gable specimen capacities were evaluated by relating multiple intensity measures, *PBA*, *PRA*, and $S_{a,avg}$ (as defined in Section 3.3), to the peak absolute value of the control-point displacement. Two displacement measures were considered: *CPD*, defined as the control-point displacement with the rigid-body motion between top and bottom tables removed, already introduced in Section 4.1 (Fig. 14a); and CPD_Δ, defined as the control-point displacement including the rigid-body motion (Δ_d, Table 3) induced by the differential table input (Fig. 14b). For each gable, the peak values of *CPD* and CPD_Δ recorded immediately before loss of equilibrium are indicated in the figures. The capacity curves are not extended up to these last points to better highlight the initial stiffness and the subsequent stiffness degradation of the specimens. Note that for clarity and continuity of the curves, Test #6-R of Gable3-FLEX is omitted.

A comparison of the capacity curves highlights the strong influence of roof-diaphragm flexibility on the seismic response of URM gables. For a given *PBA*, increasing roof flexibility leads to significantly larger OOP displacements and to a marked reduction in collapse capacity, with Gable3-FLEX exhibiting the lowest acceleration capacity and the highest deformation demand. When $S_{a,avg}$ is considered, the responses of Gable1-STIFF and Gable2-SEMIFLEX remain relatively close: for the same intensity measure level, the semi-flexible configuration exhibits slightly larger displacements and a lower $S_{a,avg}$ sustained, consistent with its amplified but in-phase ridge motion. Gable3-FLEX, instead, shows a significantly lower $S_{a,avg}$ capacity and a much more pronounced flexibility, reflecting the unfavourable influence of the amplified and out-of-phase input motion at the ridge.

On the other hand, when the seismic demand is expressed in terms of *PRA*, the capacity curves of the three gable specimens appear

substantially closer to each other. As shown in the central panels of Fig. 14, the *PRA-CPD* and *PRA-CPD*$_\Delta$ relationships exhibit reduced dispersion among the three roof-diaphragm scenarios. This behaviour indicates that similar displacement demands and damage states are reached at comparable levels of *PRA*, for all the roof-diaphragm scenarios. Expressing the seismic demand in terms of *PRA* therefore provides a representation that is more directly related to the effective acceleration demand governing the gable OOP response, as it implicitly accounts for the amplification effects along the gable height due to diaphragm flexibility. However, this observation should be interpreted considering the specific boundary conditions adopted in the present study. The tested gables were intentionally detailed without mechanical roof-to-masonry anchors, and their response was governed by frictional sliding at the timber-masonry interfaces. Under these conditions, the acceleration demand at the ridge level directly controls the activation of sliding and the subsequent rocking response; in the presence of mechanical roof-to-wall anchors, this direct relationship may no longer be valid.

The reduced sensitivity of PRA-based capacity curves to roof stiffness therefore reflects the fact that increasing diaphragm flexibility leads to progressively larger amplification of the motion transmitted to the gable ridge, which in turn governs the effective out-of-plane demand. As a result, *PRA* captures a similar level of seismic demand at collapse for all three specimens, whereas representations based on *PBA* (or $S_{a,avg}$) emphasise the unfavourable effect of roof flexibility on gable vulnerability. From this perspective, *PRA* emerges as a particularly effective intensity measure for characterising the OOP seismic capacity of URM gables with limited mechanical roof-to-wall restraint, where the non-linear response is strongly influenced by frictional sliding at the roof-masonry interfaces.

It is worth noting that, given the non-zero Δ_d values observed throughout the Gable1-STIFF testing sequence, a fully rigid diaphragm condition would be expected to yield a higher collapse acceleration at the gable base than that measured here, further increasing the dispersion among the PBA-based capacity curves. The PRA-based representation, however, would likely remain unaffected, as for a fully rigid configuration PRA coincides with PBA.

Overall, the capacity curves are consistent with the damage-state evolution discussed in Section 4.1. Gable1-STIFF responded essentially elastically from Test #1 to Test #13; the first pronounced stiffness reduction occurred only after Test #14, coinciding with the transition to DS3. Gable2-SEMIFLEX showed an almost elastic behaviour up to Test #8, followed by a slight stiffness reduction after Test #9 while still in DS2, and a more marked degradation at Test #11, when DS3 was reached. In contrast, Gable3-FLEX remained approximately elastic up to Test #8, whereas a significant stiffness drop is observed after Test #9, during which the specimen transitioned directly from DS2 to DS4.

5. Concluding remarks

This paper presented the experimental results of incremental dynamic shake-table tests conducted on three full-scale unreinforced masonry (URM) gables up to collapse. The experiments were performed using an innovative dual shake-table setup that enabled independent control of the motions at the gable base and ridge. This arrangement allowed reproducing differential input motions associated with different roof-diaphragm stiffness conditions without physically including a roof diaphragm, while still capturing the effects of motion amplification and phase differences on the out-of-plane (OOP) response. The tested specimens simulated, respectively, a stiff, semi-flexible, and flexible roof diaphragm. The evolution of the fundamental period of the gables was also monitored throughout the testing sequence.

The experimental results clearly demonstrate that roof stiffness plays a decisive role in the OOP seismic vulnerability of masonry gables. Although the three specimens were geometrically identical and subjected to the same overburden stress, and exhibited comparable peak strengths mainly governed by frictional resistance at the timber-masonry interfaces, their collapse occurred at markedly different levels of seismic demand at the attic-floor level (i.e., gable base): the stiff-diaphragm configuration collapsed at 2.33 g, the semi-flexible configuration at 1.17 g, and the flexible configuration at 0.86 g. These reductions, approximately 50% from stiff to semi-flexible and an additional 27% from semi-flexible to flexible, correspond to an overall reduction of 63% in collapse acceleration at the gable base from the stiff to the flexible roof-diaphragm configurations. This trend reflects the increasing influence of motion amplification along the gable height and, most critically, the presence of a phase shift between base and ridge motions in the most flexible setup.

All specimens failed through a consistent three-body rocking mechanism governed by one-way bending, characterised by the formation of two horizontal flexural cracks at the purlin levels, which defined the hinge lines controlling collapse. Before the development of these cracks, the gables exhibited a two-way bending response due to the restraint of the inclined sides by the timber purlins, a behaviour particularly evident in the stiff-diaphragm configuration. Once the horizontal cracks became continuous, the response transitioned from two-way bending to a one-way rocking mechanism.

The hysteretic response in all cases was dominated by frictional sliding at the timber-masonry interfaces, which controlled both energy dissipation and the onset of non-linear behaviour. Significant differences, however, emerged in the accumulation of unrecovered sliding. The stiff-diaphragm specimen showed limited residual offsets and comparatively stable loops, whereas the semi-flexible and flexible specimens developed substantial residual sliding displacements after the initiation of cracking, leading to progressively shifted and distorted hysteretic cycles. These trends reflect a systematic loss of compatibility between the gable and the purlins as diaphragm flexibility increases.

The comparison of the capacity curves further clarifies the governing role of roof-gable interaction for the tested configurations, characterised by the absence of mechanical roof-to-wall anchors and by a non-linear response largely governed by frictional sliding at the interfaces between timber purlins and masonry. When the seismic demand is expressed in terms of the acceleration at the gable base, increasing diaphragm flexibility leads to a pronounced reduction in collapse capacity and to significantly larger displacement demand. In contrast, when the demand is referred to the acceleration transmitted to the gable ridge, the capacity curves of the three configurations become markedly closer, not only at collapse but throughout the non-linear response range. This suggests that comparable levels of OOP damage and displacement demand are associated with similar acceleration levels at the gable ridge. Accordingly, expressing the seismic demand in terms of ridge acceleration provides a description that is more directly related to the effective demand acting on the gable, as it inherently incorporates the amplification effects induced by diaphragm flexibility.

Overall, the generated dataset provides a foundation for the calibration and validation of numerical models, enabling the investigation of differential input motions and the associated drift demands between gable base and ridge, and can support the development of both detailed non-linear simulations and simplified analytical formulations for improved assessment of the OOP seismic performance of URM gables. Future investigations could address alternative roof-gable connection details (e.g., presence of steel anchors or ring beams), different diaphragm stiffness configurations, and varying vertical load levels. The present results were obtained on single-leaf clay brick masonry specimens; extending the investigation to other masonry typologies (such as multi-leaf or irregular stone masonry, for which different failure mechanisms, including leaf separation or material disaggregation, may govern the OOP response prior to the activation of rocking) represents an additional important direction. These experimental and numerical developments would ultimately contribute to improved predictive tools and assessment guidelines for the out-of-plane seismic performance of URM buildings in seismic-prone regions.

CRediT authorship contribution statement

Nicolò Damiani: Writing – review & editing, Writing – original draft, Visualization, Validation, Investigation, Formal analysis, Data curation. **Satyadhrik Sharma:** Writing – review & editing, Investigation, Formal analysis, Data curation. **Marta Bertassi:** Writing – original draft, Visualization, Investigation, Formal analysis, Data curation. **Marco Smerilli:** Investigation, Data curation. **Michele Mirra:** Writing – review & editing, Investigation. **Igor Lanese:** Resources, Investigation. **Elisa Rizzo Parisi:** Resources, Investigation. **Gerard J. O'Reilly:** Writing – review & editing, Resources, Funding acquisition. **Francesco Messali:** Writing – review & editing, Supervision, Project administration, Funding acquisition. **Francesco Graziotti:** Writing – review & editing, Supervision, Methodology, Conceptualization.

Declaration of Competing Interest

The authors declare that they have no known competing financial interests or personal relationships that could have appeared to influence the work reported in this paper.

Acknowledgements

This work is part of the transnational access project "ERIES-SUPREME", supported by the Engineering Research Infrastructures for European Synergies (ERIES) project (www.eries.eu), which has received funding from the European Union's Horizon Europe Framework Programme under Grant Agreement No. 101058684. This is ERIES publication number J24. Additional funds required beyond the scope of the ERIES grant for the realisation of the project were provided by the partner TNO: Netherlands Organisation for Applied Scientific Research - Nederlandse Organisatie voor Toegepast Natuurwetenschappelijk Onderzoek. The contribution of Mario de Rooij (TNO) in managing the project is gratefully acknowledged.

Data Availability

The experimental data supporting this study are openly available in the Built Environment Data Experiments repository: https://doi.org/10.60756/euc-1avy7q49.

References

[1] Zhao B, Taucer F, Rossetto T. Field investigation on the performance of building structures during the 12 May 2008 Wenchuan earthquake in China. Eng Struct 2009;31:1707–23. https://doi.org/10.1016/j.engstruct.2009.02.039.
[2] Rossetto T, Peiris N. Observations of damage due to the Kashmir earthquake of October 8, 2005 and study of current seismic provisions for buildings in Pakistan. Bull Earthq Eng 2009;7:681–99. https://doi.org/10.1007/s10518-009-9118-5.
[3] Yon B, Sayın E, Koksal TS. Seismic response of buildings during the May 19, 2011 Simav, Turkey earthquake. Earthq Struct 2013;5:343–57. https://doi.org/10.12989/eas.2013.5.3.343.
[4] Ural A, Doğangün A, Sezen H, Angın Z. Seismic performance of masonry buildings during the 2007 Bala, Turkey earthquakes. Nat Hazards 2012;60:1013–26. https://doi.org/10.1007/s11069-011-9887-4.
[5] Sayın E, Yön B, Calayır Y, Karaton M. Failures of masonry and adobe buildings during the June 23, 2011 Maden-(Elazığ) earthquake in Turkey. Eng Fail Anal 2013;34:779–91. https://doi.org/10.1016/j.engfailanal.2012.10.016.
[6] Sayin E, Yon B, Calayir Y, Gor M. Construction failures of masonry and adobe buildings during the 2011 Van earthquakes in Turkey. Struct Eng Mech 2014;51:503–18. https://doi.org/10.12989/sem.2014.51.3.503.
[7] Mercimek Ö. Seismic failure modes of masonry structures exposed to Kahramanmaraş earthquakes (Mw 7.7 and 7.6) on February 6, 2023. Eng Fail Anal 2023;151:107422. https://doi.org/10.1016/j.engfailanal.2023.107422.
[8] Kocaman İ. Damage mechanisms of masonry structures: an observation after 19 November Erzurum-Köprüköy Earthquake. J Struct Eng & Appl Mech 2023;6:455–67. https://doi.org/10.31462/jseam.2023.05455467.
[9] Inel M, Ozmen HB, Akyol E. Observations on the building damages after 19 May 2011 Simav (Turkey) earthquake. Bull Earthq Eng 2013;11:255–83. https://doi.org/10.1007/s10518-012-9414-3.
[10] Celep Z, Erken A, Taskin B, Ilki A. Failures of masonry and concrete buildings during the March 8, 2010 Kovancılar and Palu (Elazığ) Earthquakes in Turkey. Eng Fail Anal 2011;18:868–89. https://doi.org/10.1016/j.engfailanal.2010.11.001.
[11] Calayır Y, Sayın E, Yön B. Performance of structures in the rural area during the March 8, 2010 Elazığ-Kovancılar earthquake. Nat Hazards 2012;61:703–17. https://doi.org/10.1007/s11069-011-0056-6.
[12] Bayraktar A, Coşkun N, Yalçin A. Performance of Masonry Stone Buildings during the March 25 and 28, 2004 Aşkale (Erzurum) Earthquakes in Turkey. J Perform Constr Facil 2007;21:432–40. https://doi.org/10.1061/(ASCE)0887-3828(2007)21:6(432).
[13] Ingham J, Griffith M. Performance of Unreinforced Masonry Buildings During the 2010 Darfield (Christchurch, Nz) Earthquake. Aust J Struct Eng 2010;11:207–24. https://doi.org/10.1080/13287982.2010.11465067.
[14] Sharma K, Deng L, Noguez CC. Field investigation on the performance of building structures during the April 25, 2015, Gorkha earthquake in Nepal. Eng Struct 2016;121:61–74. https://doi.org/10.1016/j.engstruct.2016.04.043.
[15] Decanini L, De Sortis A, Goretti A, Langenbach R, Mollaioli F, Rasulo A. Performance of Masonry Buildings during the 2002 Molise, Italy, Earthquake. Earthq Spectra 2004;20:191–220. https://doi.org/10.1193/1.1765106.
[16] Ahmadizadeh M, Shakib H. On the December 26, 2003, southeastern Iran earthquake in Bam region. Eng Struct 2004;26:1055–70. https://doi.org/10.1016/j.engstruct.2004.03.006.
[17] Hafner I, Lazarević D, Kišiček T, Stepinac M. Post-Earthquake Assessment of a Historical Masonry Building after the Zagreb Earthquake—Case Study. Buildings 2022;12:323. https://doi.org/10.3390/buildings12030323.
[18] Penna A, Calderini C, Sorrentino L, Carocci CF, Cescatti E, Sisti R, et al. Damage to churches in the 2016 central Italy earthquakes. Bull Earthq Eng 2019;17:5763–90. https://doi.org/10.1007/s10518-019-00594-4.
[19] Lagomarsino S. Damage assessment of churches after L'Aquila earthquake (2009). Bull Earthq Eng 2012;10:73–92. https://doi.org/10.1007/s10518-011-9307-x.
[20] Binda L, Chesi C, Parisi MA. Seismic Damage to Churches: Observations from the L'Aquila, Italy, Earthquake and Considerations on a Case-Study. Adv Mat Res 2010;133–134:641–6. https://doi.org/10.4028/www.scientific.net/AMR.133-134.641.
[21] Augenti N, Parisi F. Learning from Construction Failures due to the 2009 L'Aquila, Italy, Earthquake. J Perform Constr Facil 2010;24:536–55. https://doi.org/10.1061/(ASCE)CF.1943-5509.0000122.
[22] Degli Abbati S, Lagomarsino S. Out-of-plane static and dynamic response of masonry panels. Eng Struct 2017;150:803–20. https://doi.org/10.1016/j.engstruct.2017.07.070.
[23] Ghezelbash A, Sharma S, Rots JG, Messali F. Effect of relative support motions on the out-of-plane dynamics of one-way spanning unreinforced masonry walls and insights into their instability displacement. J Struct Eng 2026. https://doi.org/10.1061/JSENDH/STENG-15104.
[24] Griffith MC, Lam NTK, Wilson JL, Doherty K. Experimental Investigation of Unreinforced Brick Masonry Walls in Flexure. J Struct Eng 2004;130:423–32. https://doi.org/10.1061/(ASCE)0733-9445(2004)130:3(423).
[25] Penner O, Elwood KJ. Out-of-Plane Dynamic Stability of Unreinforced Masonry Walls in One-Way Bending: Parametric Study and Assessment Guidelines. Earthq Spectra 2016;32:1699–723. https://doi.org/10.1193/011715EQS011M.
[26] Giaretton M, Dizhur D, Ingham JM. Dynamic testing of as-built clay brick unreinforced masonry parapets. Eng Struct 2016;127:676–85. https://doi.org/10.1016/j.engstruct.2016.09.016.
[27] Graziotti F, Tomassetti U, Penna A, Magenes G. Out-of-plane shaking table tests on URM single leaf and cavity walls. Eng Struct 2016;125:455–70. https://doi.org/10.1016/j.engstruct.2016.07.011.
[28] Sharma S, Tomassetti U, Grottoli L, Graziotti F. Two-way bending experimental response of URM walls subjected to combined horizontal and vertical seismic excitation. Eng Struct 2020;219:110537. https://doi.org/10.1016/j.engstruct.2020.110537.
[29] Tomassetti U, Grottoli L, Sharma S, Graziotti F. Dataset from dynamic shake-table testing of five full-scale single leaf and cavity URM walls subjected to out-of-plane two-way bending. Data Brief 2019;24:103854. https://doi.org/10.1016/j.dib.2019.103854.
[30] Sharma S, Grottoli L, Tomassetti U, Graziotti F. Dataset from shake-table testing of four full-scale URM walls in a two-way bending configuration subjected to combined out-of-plane horizontal and vertical excitation. Data Brief 2020;31:105851. https://doi.org/10.1016/j.dib.2020.105851.
[31] Graziotti F, Tomassetti U, Sharma S, Grottoli L, Magenes G. Experimental response of URM single leaf and cavity walls in out-of-plane two-way bending generated by seismic excitation. Constr Build Mater 2019;195:650–70. https://doi.org/10.1016/j.conbuildmat.2018.10.076.
[32] Tomassetti U, Correia AA, Graziotti F, Penna A. Seismic vulnerability of roof systems combining URM gable walls and timber diaphragms. Earthq Eng Struct Dyn 2019;48:1297–318. https://doi.org/10.1002/eqe.3187.
[33] Candeias PX, Costa AC, Mendes N, Costa AA, Lourenço PB. Experimental Assessment of the Out-of-Plane Performance of Masonry Buildings Through Shaking Table Tests. Int J Archit Herit 2016:1–28. https://doi.org/10.1080/15583058.2016.1238975.
[34] Magenes G, Penna A, Senaldi IE, Rota M, Galasco A. Shaking Table Test of a Strengthened Full-Scale Stone Masonry Building with Flexible Diaphragms. Int J Archit Herit 2014;8:349–75. https://doi.org/10.1080/15583058.2013.826299.
[35] Guerrini G, Senaldi I, Graziotti F, Magenes G, Beyer K, Penna A. Shake-Table Test of a Strengthened Stone Masonry Building Aggregate with Flexible Diaphragms. Int J Archit Herit 2019;13:1078–97. https://doi.org/10.1080/15583058.2019.1635661.
[36] Graziotti F, Tomassetti U, Kallioras S, Penna A, Magenes G. Shaking table test on a full scale URM cavity wall building. Bull Earthq Eng 2017;15:5329–64. https://doi.org/10.1007/s10518-017-0185-8.

[37] Kallioras S, Graziotti F, Penna A, Magenes G. Effects of vertical ground motions on the dynamic response of URM structures: Comparative shake-table tests. Earthq Eng Struct Dyn 2022;51:347–68. https://doi.org/10.1002/eqe.3569.
[38] Miglietta M, Damiani N, Guerrini G, Graziotti F. Full-scale shake-table tests on two unreinforced masonry cavity-wall buildings: effect of an innovative timber retrofit. Bull Earthq Eng 2021;19:2561–96. https://doi.org/10.1007/s10518-021-01057-5.
[39] Kallioras S, Correia AA, Graziotti F, Penna A, Magenes G. Collapse shake-table testing of a clay-URM building with chimneys. Bull Earthq Eng 2020;18:1009–48. https://doi.org/10.1007/s10518-019-00730-0.
[40] Tomassetti U, Correia AA, Candeias PX, Graziotti F, Campos Costa A. Two-way bending out-of-plane collapse of a full-scale URM building tested on a shake table. Bull Earthq Eng 2019;17:2165–98. https://doi.org/10.1007/s10518-018-0507-5.
[41] Shahnazaryan D, Pinho R, Crowley H. G.J. O'Reilly, The Built Environment Data platform for experimental test data in earthquake engineering. Earthq Eng Struct Dyn 2024;53:4627–40. https://doi.org/10.1002/eqe.4231.
[42] Sharma S, Damiani N, Bertassi M, Smerilli M, Mirra M, Lanese I, et al. Experimental data from out-of-plane shake-table tests on unreinforced masonry gables. Earthq Spectra 2025. https://doi.org/10.1177/87552930251378248.
[43] Arslan O, Messali F, Smyrou E, Bal İE, Rots JG. Characterisation of timber joists-masonry connections in double-leaf cavity walls – Part 1: Experimental results. Structures 2024;68:107164. https://doi.org/10.1016/j.istruc.2024.107164.
[44] Mirra M, Ravenshorst G, de Vries P, Messali F. Experimental characterisation of as-built and retrofitted timber-masonry connections under monotonic, cyclic and dynamic loading. Constr Build Mater 2022;358:129446. https://doi.org/10.1016/j.conbuildmat.2022.129446.
[45] Dizhur D, Moon L, Ingham J. Observed Performance of Residential Masonry Veneer Construction in the 2010/2011 Canterbury Earthquake Sequence. Earthq Spectra 2013;29:1255–74. https://doi.org/10.1193/050912EQS185M.
[46] A.A. Correia, U. Tomassetti, A. Campos Costa, A. Penna, G. Magenes, F. Graziotti, Collapse shake-table test on a URM-timber roof substructure, in: Proceedings of the 16th European Conference on Earthquake Engineering, 16ECEE, Thessaloniki, Greece, 2018: pp. 18–21.
[47] Tomassetti U, Correia AA, Graziotti F, Penna A. Seismic vulnerability of roof systems combining URM gable walls and timber diaphragms. Earthq Eng Struct Dyn 2019;48:1297–318. https://doi.org/10.1002/eqe.3187.
[48] European Committee for Standardization, Methods of test for masonry units. Part 1: Determination of compressive strength. European Standard EN 772-1, Brussels, Belgium, 2011.
[49] European Committee for Standardization (CEN), Methods of test for mortar for masonry. Part 11: Determination of flexural and compressive strength of hardened mortar. European Standard EN 1015-11, Brussels, Belgium, 2006.
[50] European Committee for Standardization (CEN), Methods of test for masonry. Part 1: Determination of compressive strength. European Standard EN 1052-1, Brussels, Belgium, 1998.
[51] European Committee for Standardization (CEN), Methods of test for masonry units. Part 3: Determination of initial shear strength. European Standard EN 1052-3, Brussels, Belgium, 2007.
[52] European Committee for Standardization (CEN), Methods of test for masonry. Part 5: Determination of bond strength by the Bond Wrench method. European Standard EN 1052-5, Brussels, Belgium, 2005.
[53] Sharma S, Graziotti F, Magenes G. Torsional shear strength of unreinforced brick masonry bed joints. Constr Build Mater 2021;275:122053. https://doi.org/10.1016/j.conbuildmat.2020.122053.
[54] Mirra M, Damiani N, Sharma S, Graziotti F, Messali F. Definition of differential seismic input motions for out-of-plane dynamic testing of unreinforced masonry gable walls considering different roof configurations. Structures 2025;79:109419. https://doi.org/10.1016/j.istruc.2025.109419.
[55] Kohrangi M, Bazzurro P, Vamvatsikos D, Spillatura A. Conditional spectrum-based ground motion record selection using average spectral acceleration. Earthq Eng Struct Dyn 2017;46:1667–85. https://doi.org/10.1002/eqe.2876.
[56] MIDAS Information Technology Co., MIDAS Gen – General Structure Design System, 2024. https://www.midasuser.com/en/product/gen.
[57] Itasca Consulting Group Inc., 3DEC "Three Dimensional Distinct Element Code", 2024. https://docs.itascacg.com/itasca910/3dec/docproject/source/3dechome.html.